VIROLOGY

The structurally disordered paramyxovirus nucleocapsid protein tail domain is a regulator of the mRNA transcription gradient

Robert M. Cox,[1] Stefanie A. Krumm,[1] Vidhi D. Thakkar,[1] Maximilian Sohn,[2] Richard K. Plemper[1,2]*

The paramyxovirus RNA-dependent RNA-polymerase (RdRp) complex loads onto the nucleocapsid protein (N)–encapsidated viral N:RNA genome for RNA synthesis. Binding of the RdRp of measles virus (MeV), a paramyxovirus archetype, is mediated through interaction with a molecular recognition element (MoRE) located near the end of the carboxyl-terminal Ntail domain. The structurally disordered central Ntail section is thought to add positional flexibility to MoRE, but the functional importance of this Ntail region for RNA polymerization is unclear. To address this question, we dissected functional elements of Ntail by relocating MoRE into the RNA-encapsidating Ncore domain. Linker-scanning mutagenesis identified a microdomain in Ncore that tolerates insertions. MoRE relocated to Ncore supported efficient interaction with N, MoRE-deficient Ntails had a dominant-negative effect on bioactivity that was alleviated by insertion of MoRE into Ncore, and recombinant MeV encoding N with relocated MoRE grew efficiently and remained capable of mRNA editing. MoRE in Ncore also restored viability of a recombinant lacking the disordered central Ntail section, but this recombinant was temperature-sensitive, with reduced RdRp loading efficiency and a flattened transcription gradient. These results demonstrate that virus replication requires high-affinity RdRp binding sites in N:RNA, but productive RdRp binding is independent of positional flexibility of MoRE and cis-acting elements in Ntail. Rather, the disordered central Ntail section independent of the presence of MoRE in Ntail steepens the paramyxovirus transcription gradient by promoting RdRp loading and preventing the formation of nonproductive polycistronic viral mRNAs. Disordered Ntails may have evolved as a regulatory element to adjust paramyxovirus gene expression.

INTRODUCTION

Paramyxoviruses are enveloped RNA viruses that are collectively responsible for major human and animal morbidity and mortality worldwide (*1*). In addition to measles virus (MeV), an archetype member of the family and member of the morbillivirus genus, the paramyxoviruses comprise major respiratory pathogens, such as mumps virus (MuV), the parainfluenzaviruses (PIVs), Nipah (NiV) and Hendra (HeV) viruses, and canine distemper virus (CDV). Being part of the order mononegavirales, paramyxoviruses feature nonsegmented negative-stranded genomes that are encapsidated by the viral N protein, resulting in the formation of helical N:RNA ribonucleoprotein assemblies (*2*–*5*). Only the encapsidated RNA is recognized as a template by the viral RNA-dependent RNA-polymerase (RdRp) complex that is responsible for both transcription and replication of all viral RNA (*6*–*8*). Genome and antigenome encapsidation occurs concomitant to RNA synthesis, and RdRp switches into replicase mode only after a sufficiently large pool of N protein has been generated in infected cells (*1*, *5*, *9*).

Key components of the RdRp complex are the viral polymerase (L) protein and its essential cofactor, the phosphoprotein (P). The L protein mediates all enzymatic activities required for mRNA synthesis and genome production, such as nucleotide polymerization, mRNA capping, polyadenylation, and methylation, but does not interact directly with N:RNA. Rather, the P protein interacts with N and is thought to stabilize attachment of the advancing polymerase to the N:RNA (*10*–*16*) and also to deliver free N proteins to the replicase complex for encapsidation of the nascent strand (*17*–*20*). The MeV P protein is composed of an N-terminal (PNT) domain (amino acids 1 to 230) and a C-terminal (PCT) domain (amino acids 231 to 507). PNT is responsible for this chaperoning of newly synthesized N proteins to the replicase, holding N monomers in an open conformation and preventing premature oligomerization (*19*, *20*). Major structural domains in PCT include a tetramerization domain mediating homo-oligomerization and a C-terminal N:RNA binding domain (P-XD) (*10*, *11*, *21*–*23*) that mediates high-affinity interactions with the N protein.

MeV N itself consists of a conserved core domain (Ncore) spanning residues 1 to 400 that mediates homo-oligomerization and RNA binding, and a 125–amino acid tail domain (Ntail) that protrudes from the surface of the assembled viral N:RNA (*5*, *24*). Ncore determines the spatial organization of the helical N:RNA complex, as evidenced by the atomic structures of the NiV, PIV5, and MeV Ncores that were recently solved (*19*, *20*, *25*, *26*). In all cases, these structures revealed a separation of Ncore into an N-terminal and a C-terminal section that are separated by a groove accommodating the encapsidated RNA.

Although the MeV Ntail has not returned defined electron density in the N:RNA reconstruction and is considered to be largely structurally disordered (*12*, *27*–*30*), the presence of the tail affects the overall spatial organization of N:RNA. Complete removal of Ntail by trypsin digestion decreases MeV N:RNA diameter and pitch, leading to increased rigidity (*31*) and the elimination of bioactivity. Multiple studies have suggested that the Ntail protrudes through the interstitial space between successive turns of the N:RNA helix, leaving approximately 50 amino acids buried inside the helix and only the terminal residues 450 to 525 exposed on the N:RNA surface (*10*, *28*, *30*). Although most of the central region of the morbillivirus Ntail is predicted to be disordered, three conserved microdomains or boxes have been identified (*32*). These comprise the N-terminal box 1 (residues 400 to 420) and the C-terminal box 2 (residues 589 to 506) and

[1]Institute for Biomedical Sciences, Georgia State University, Atlanta, GA 30303, USA. [2]Department of Pediatrics, Emory University School of Medicine, Atlanta, GA 30322, USA.
*Corresponding author. Email: rplemper@gsu.edu

box 3 (residues 517 to 525). Located within box 2 is an α-helical molecular recognition element (MoRE; residues 488 to 499).

Box 1 has been hypothesized to bind a cellular receptor (*33*, *34*), but the nature of this receptor has remained obscure and the predicted position of box 1 between the rungs of the helical N:RNA makes its availability for protein-protein interactions doubtful. Functional roles have been defined for both boxes 2 and 3. The former is thought to mediate high-affinity interactions with RdRp by engaging P-XD (*10*, *12*, *13*, *22*), while the latter contributes to genome incorporation into nascent virions through direct interaction with the viral matrix (M) protein (*35*, *36*). In addition, box 3 is thought to interact with cellular factors such as hsp70, which has been postulated to facilitate separation of MoRE and P-XD through cis-acting modulatory effects, enabling the RdRp complex to proceed along the genome (*37*, *38*).

Two major roles in polymerase activity were originally attributed to this MoRE:P-XD interaction: initial loading of the RdRp complex onto the genome and prevention of premature termination of polymerization by tethering the advancing polymerase complex to the template (*5*, *29*, *39*). However, a recent study showed that deletion of the 86 C-terminal amino acids, including boxes 2 and 3 and all surface-exposed residues of the unstructured central Ntail section, retained approximately 60% of standard MeV N bioactivity in minigenome assays, ruling out the possibility that MoRE is fundamentally required for RdRp loading onto the N:RNA template (*23*). Despite the considerable bioactivity in minigenome assays, recombinant MeV encoding this truncated N protein in place of standard N could not be recovered in this study. These data suggested that the MoRE:P-XD interaction is required to successfully master the greater template length of the viral genome compared to a minireplicon reporter, preventing catastrophic premature polymerase termination (*23*).

Although these emerging data have begun to elucidate the contribution of the MoRE:P-XD interaction to polymerase activity, the functional role of the unstructured central Ntail section in paramyxovirus RNA replication is not understood. It was suggested that this section may provide positional flexibility of MoRE relative to the trunk of the N:RNA helix, which is thought to facilitate the critical random encounter between MoRE and P-XD through a fly-casting mechanism (*40*) that allows the formation of high-affinity complexes. However, previous studies of recombinant virions to test these models were limited to the characterization of individual mutations inserted into the box 2 and/or 3 domains (*36*, *37*, *39*, *41*), which imposes shortcomings: These studies are, by design, unable to explore the mechanistic importance of the disordered Ntail sections for polymerization, and the interpretation of results is compromised by the possibility that uncharacterized cis-acting elements in Ntail may enhance or alleviate the effect of individual mutations. Thus, the multidomain architecture of the Ntail and the unstructured nature of the central Ntail section itself have prevented its functional characterization because it has been impossible to separate the contribution of the central section to polymerization from that of the MoRE:P-XD interaction.

Overcoming this obstacle was therefore the first aim of the present study. We developed a strategy to dissect Ntail into distinct functional elements while preserving bioactivity in both minigenome assays and the context of recombinant virus replication as the premise for the subsequent mechanistic characterization of the role of the individual Ntail elements in paramyxovirus replication. Relocating MoRE into Ncore may have allowed us to revert MeV to use an ancient mode of N:RNA interaction (if the docking of P to a binding site in Ncore indeed represents the evolutionary older form of interaction).

RESULTS

Bioinformatics analyses have predicted several unstructured and disordered regions in the morbillivirus N protein (*42*, *43*). In search of candidate Ncore sites that tolerate domain insertions, we enhanced the resolution of these previous domain predictions by subjecting the MeV N protein to a comprehensive meta-analysis of structurally disordered linker regions using a panel of distinct structure prediction algorithms. The individual in silico predictions were cross-referenced quantitatively, and the results were graphically plotted as a function of MeV-Edm N (Fig. 1A). In addition to the N terminus and the complete C-terminal Ntail, this analysis highlighted a microdomain in the N-terminal half of Ncore (residues 110 to 145) as a candidate interdomain region. A structural disorder analysis of N proteins derived from representatives of all mononegavirales revealed that this pattern was mirrored by several families within the order, with the exception of the rhabdo- and pneumoviruses, which both completely lack a disordered Ntail domain (Fig. 1B).

Insertion scanning analysis of the nucleoprotein

To experimentally test the validity of the N protein domain architecture predictions, we launched a comprehensive linker insertion analysis, adding four amino acid peptide linkers (sequence GDAS) throughout the N protein in approximately 10– to 20–amino acid intervals, guided where possible by the local in silico predictions. Steady-state levels of all resulting N mutants were evaluated through immunoblotting after transient expression. Linker insertions were best tolerated throughout Ntail and, to some extent, in the N-terminal half of Ncore, whereas most mutants with an insertion in the C-terminal half of Ncore were barely detectable, suggesting severe misfolding followed by degradation (Fig. 1C). To assess the impact of linker insertions on N bioactivity, the mutants were tested in parallel in a monocistronic MeV minigenome assay (*44*) using a firefly luciferase reporter to monitor RdRp transcriptase function (Fig. 1D). All N constructs harboring linker insertions in the Ntail maintained bioactivities from 70 to 130% that of standard N, underscoring the unstructured nature of the Ntail (*30*, *42*, *45*, *46*). In contrast, all insertions in Ncore abolished bioactivity, with the striking exception of an Ncore microdomain spanning residues 131 to 138 (Fig. 1D). Follow-up mapping of this putative interdomain region revealed that insertions at residues 131 and 133 were best tolerated, with no adverse effect on N bioactivity. Overlay of the activity data with the average prediction scores of the in silico analysis revealed a slightly elevated disorder propensity for N residues 115 to 140, but it is noteworthy that the overall correlation between the in silico predictions and experimental data was poor for the Ncore domain (Fig. 1D).

To explore the packaging capacity of the interdomain region of N residues 131 to 138, we inserted a larger 17–amino acid peptide encoding a HA epitope tag flanked by glycine linkers (sequence SGGGYPYDVPDYAGGGS) at N positions 131 and 138, respectively. For reference, we also added this tag near the center of the flexible Ntail, at positions 436 and 469, respectively. Although both insertions in the tail were tolerated with reductions in bioactivity of less than 30% compared to standard N, introducing the tag at Ncore position 131 reduced bioactivity by approximately 90% and by 60% when placed at position 138 (Fig. 1E). These differences in bioactivity were not due to changes in protein expression rate and stability because all constructs reached comparable steady-state levels (Fig. 1F).

Relocation of MoRE into the MeV N core

On the basis of these results, we considered N position 138 as the target for relocation of a 22–amino acid fragment (QDPQDSRRSADALLRLQAMAGI)

including MoRE from Ntail. Applying in silico modeling based on the available reconstructions of standard MeV Ncore and N:RNA assemblies (*25*), we simulated the structural consequences of this relocation in the context of an individual N monomer (Fig. 2, A and B), an isolated 12-membered N ring (Fig. 2, C and D), and the helical MeV N:RNA assembly (Fig. 2, E and F). The SWISS-MODEL homology modeling server (*47*) was used to model disordered regions spanning Ncore residues 117 to 124 and 134 to 142. These simulations posited MoRE approximately 75 Å closer to the N:RNA helix trunk from its natural location near the end of the unstructured Ntails (measurement based on radial extension of Ntail from the N:RNA helix trunk) and predicted that lateral flexibility of the element is markedly restricted compared to standard N.

To explore MoRE relocation in cellula, we generated five different N mutants in addition to the previously described N-Δ86 construct that lacks the 86 C-terminal residues of N (Fig. 3A). First, we added

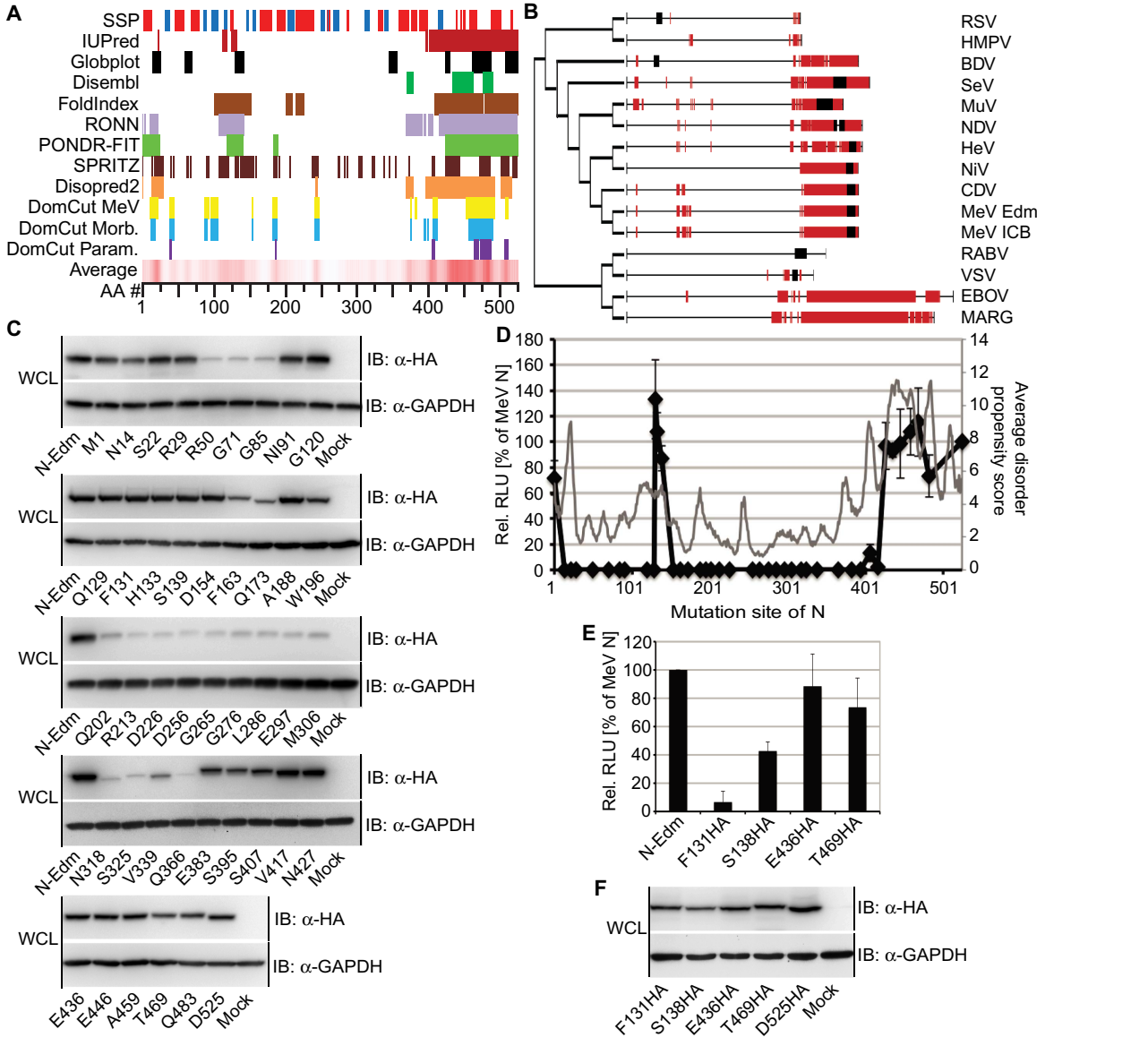

Fig. 1. Identification of an interdomain linker region in MeV N that tolerates peptide insertions. (**A**) Top: Distinct algorithms to predict unstructured regions in the MeV N protein; candidate unstructured regions are color-coded. Bottom: Heat map of the quantitative average of all predictors used; numbers correspond to amino acid counts. (**B**) Phylogenetic tree of the N proteins of representatives of all five families of the mononegavirales. Candidate structurally disordered domains are highlighted in red, and known high-affinity binding sites for P-L are shown as black boxes. (**C**) Steady-state levels of N mutants generated through 4–amino acid linker-scanning mutagenesis. Whole-cell lysates (WCL) of cells transfected with N expression plasmids were gel-fractionated, and N proteins were detected using specific antibodies directed against a C-terminally inserted HA epitope. Cellular glyceraldehyde-3-phosphate dehydrogenase (GAPDH) was detected for loading control. IB, immunoblots. (**D**) Bioactivity of the linker scanning mutants, assessed in minireplicon assays (black curve) using a monocistronic MeV minigenome reporter. Values represent averages of four independent experiments ± SD. The gray curve shows average disorder propensity scores determined in (A). RLU, relative light units. (**E**) Minireplicon analysis of N mutants harboring insertions of an HA epitope tag at the specified residues in Ncore and Ntail. Averages of three independent experiments ± SD are shown. (**F**) Steady-state levels of the N mutants analyzed in (E). Immunoblots were generated and developed as in (C).

a second MoRE domain at Ncore position 138 to address whether MoRE in Ncore may have a dominant-negative effect on RdRp activity (N-2xMoRE). Second, we relocated MoRE from the tail to this Ncore position but left the Ntail architecture otherwise unchanged (Ncore-MoRE). Third, as a control, we deleted MoRE from the Ntail (N-noMoRE), resulting in an Ntail structure identical to that of Ncore-MoRE. Fourth, we added MoRE to Ncore position 138 in the context of the tail-truncated N-Δ86 variant (Ncore-MoRE-Δ86). Last, we reattached the terminal box 3 domain to the C terminus of this Ncore-MoRE-Δ86 mutant (Ncore-MoRE-Δ86-B3).

Immunoblotting of transiently expressed N demonstrated that all N mutants were expressed efficiently, reaching steady-state levels comparable to unmodified standard MeV N (Fig. 3B). As before, minireplicon assays using the conventional monocistronic minigenome revealed that Ncore-MoRE remained bioactive, supporting approximately 75% luciferase reporter activity compared to standard N. This activity level was virtually identical to that reached by N-2xMoRE, indicating that doubling the number of MoREs in N:RNA does not inhibit polymerase processivity. In contrast, eliminating MoRE from the otherwise unchanged N protein (N-noMoRE) almost entirely abrogated RdRp activity (Fig. 3C). This result was consistent with the outcome of previous studies in which Ntail was truncated immediately upstream of MoRE (*23*, *38*). As we have shown before, further Ntail shortening through truncation at position 440 (generating N-Δ86) partially restored bioactivity to approximately 65% that of standard N (*23*). The addition of MoRE to the core of N-Δ86 (Ncore-MoRE-Δ86) significantly boosted RdRp activity to levels indistinguishable to those achieved in the presence of standard N. However, addition of the conserved 8–amino acid box 3 region to the C terminus of Ncore-MoRE-Δ86 had a somewhat detrimental effect, reducing bioactivity back to the levels obtained with Ncore-MoRE and N-Δ86, respectively (Fig. 3C).

To address whether N:RNAs with relocated MoRE allow RdRp to efficiently negotiate the intergenic junctions in the viral genome, a process that involves the nontemplated polyadenylation of the newly synthesized mRNA, migration of the RdRp complex to the next downstream transcription start sequence, and reinitiation of RNA synthesis, we generated novel firefly luciferase and nanoluciferase bi- and tricistronic minigenome reporter plasmids (Fig. 3D). The bicistronic reporter harbors the N/P open reading frame (ORF) intergenic junction of the MeV

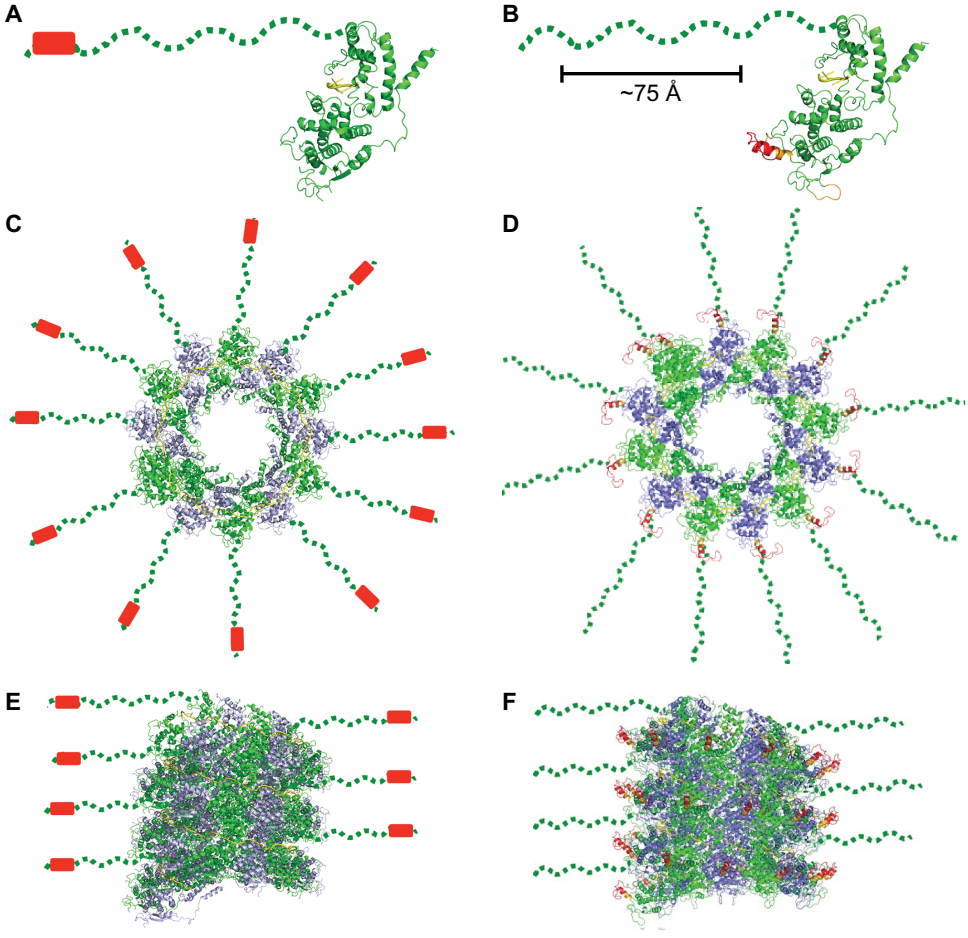

Fig. 2. Structural models of standard MeV N and N featuring MoRE relocated into Ncore. MoRE is shown as red cylinder or ribbon, respectively. (**A** and **B**) Side view of monomers of MeV N (A) [Protein Data Bank (PDB) ID: 4UFT] and MeV Ncore-MoRE (B) showing the predicted positions of MoRE in red. Residues shown in orange are predicted to be disordered in native MeV N. Compared to its position in a fully extended Ntail, relocation shifts MoRE approximately 75 Å toward Ncore. (**C** and **D**) Top views of a single rung of the helical MeV N:RNA assemblies featuring standard N (C) and Ncore-MoRE (D). N protomers are colored, alternating in green and slate; RNA is shown in yellow. Dashed lines represent fully extended Ntails, shown in straight radial extension from the helix. (**E** and **F**) Side views of internal sections of assembled N:RNA helices featuring standard N and Ncore-MoRE, as shown in (C) and (D), respectively. All images were rendered with MacPyMOL.

genome between the luciferase reporter genes, whereas the tricistronic plasmids contains the entire MeV P ORF including the N/P and P/M intergenic junctions. To avoid influencing minireplicon activity through additional P protein originating from the tricistronic minigenome, tandem stop codons were inserted into the P reading frame 21 triplets downstream of the start codon. Quantitative reverse transcription polymerase chain reaction (qRT-PCR) analysis of the relative mRNA copy numbers generated from the downstream reporter ORF relative to the upstream reporter ORF in minireplicon assays were similar to relative P versus N mRNA levels in recombinant MeV-Edmonston (recMeV)–infected

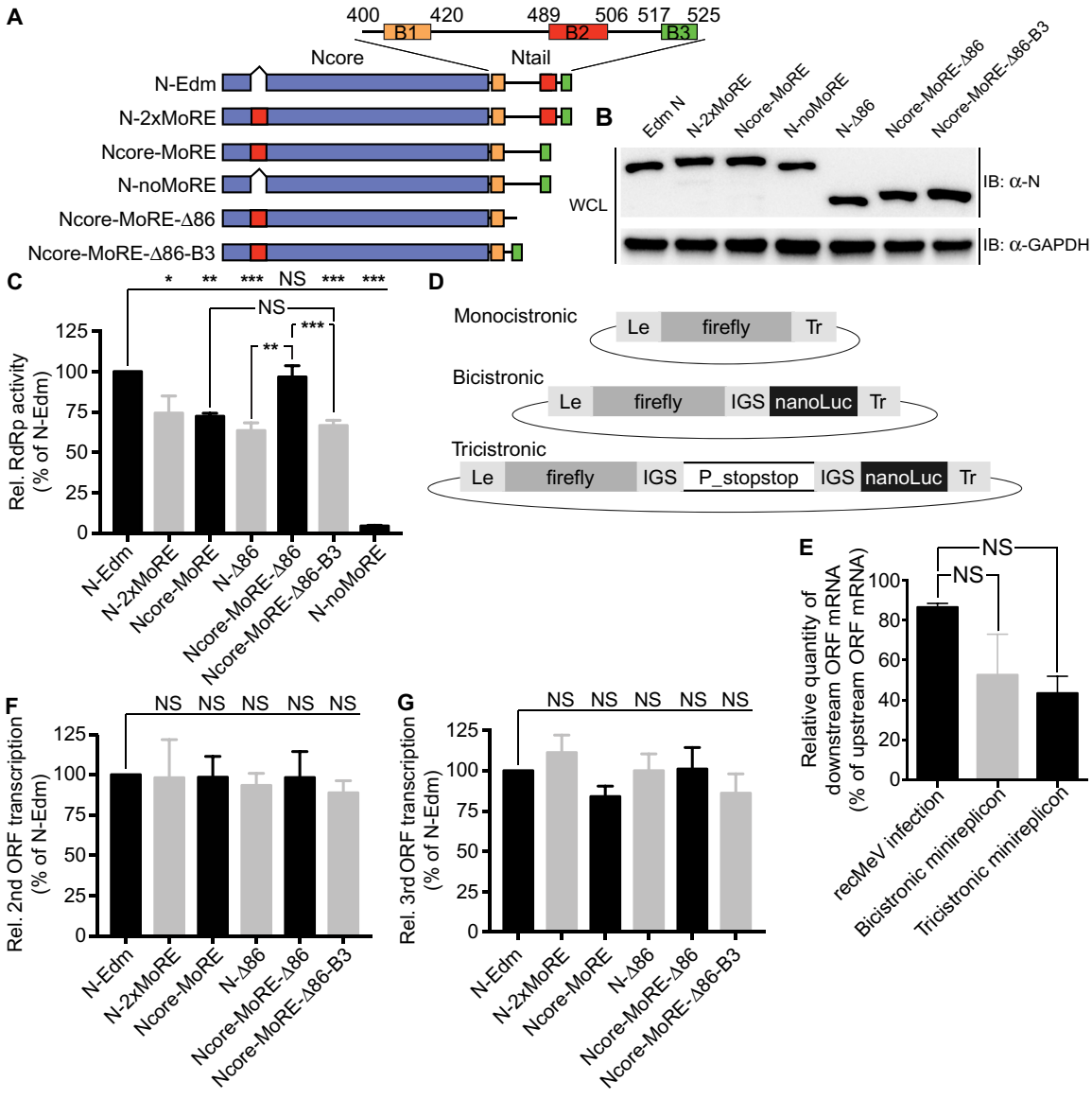

Fig. 3. Activity characterization of transiently expressed MeV N mutants. (**A**) Schematic of the MeV N protein domain organization. Conserved boxes 1 to 3 in Ntail (B1 to B3) are highlighted, and the position of MoRE inserted into Ncore (red box) is indicated. Numbers represent amino acid positions. (**B**) Steady-state levels of transiently expressed MeV N mutants schematically shown in (A). Immunoblots were prepared and analyzed as in Fig. 1C. (**C**) Minireplicon analysis of the MeV N mutants depicted in (A) using a monocistronic firefly luciferase minigenome reporter schematically shown in (D). Values represent averages of at least three independent experiments, determined in nonuplets each ± SEM. Experimental variation was assessed through one-way analysis of variance (ANOVA) combined with Sidak's multiple comparison post test (*P < 0.05; **P < 0.01; ***P < 0.001; NS, not significant). (**D**) Schematics of the bi- and tricistronic minigenome plasmids generated (firefly, firefly luciferase; nanoLuc, nanoluciferase; IGS, intergenic segment; Le, leader sequence; Tr, trailer sequence; P_stopstop, MeV P protein–encoding ORF harboring a tandem stop codon after the 21st triplet). (**E**) qRT-PCR–based comparison of transcription gradients experienced with polycistronic minireplicons versus virus infection. qRT-PCR analysis of the RNA panel shown in (C) to determine the ratios of N- and L-encoding mRNAs. Values represent the percentage of downstream ORF mRNA relative to upstream ORF mRNA in each sample (recMeV infection upstream ORF, N mRNA; downstream ORF, P mRNA; minireplicons upstream ORF, firefly luciferase mRNA; downstream ORF, nanoluciferase mRNA). Averages ± SEM of three independent experiments are shown, analyzed in duplicate each. Experimental variations were assessed through one-way ANOVAs combined with Sidak's multiple comparison post tests. (**F** and **G**) Assessment of the relative efficiency with which the downstream reporter ORF was transcribed in the presence of the different N mutants using the bicistronic (F) and tricistronic (G) minigenomes shown in (D). Relative reporter expression ratios represent averages of at least five independent experiments, determined in nonuplets each ± SEM. Experimental variation was assessed through one-way ANOVA combined with Sidak's multiple comparison post test.

cells (Fig. 3E), indicating that a transcription gradient resembling that of viral protein expression in infected cells is replicated by the polycistronic minireplicons.

For analysis of the polycistronic minigenome data, we first separately normalized the data sets obtained for each reporter for the signals obtained in the presence of standard N and then individually calculated the ratios of normalized nanoluciferase versus firefly luciferase signals for each N mutant. This approach enables us to appreciate the relative efficiency with which the RdRp complex accesses the downstream relative to the upstream reporter in the presence of the different N constructs, independent of the absolute differences in RdRp activity experienced with the different N mutants that are documented in Fig. 3C. When applied to the panel of Ncore mutants, we noted in all cases essentially unaltered firefly luciferase and nanoluciferase activity ratios compared to those observed with standard N (Fig. 3, F and G). This finding extended equally to the previously generated bioactive N-Δ86 mutant lacking any MoRE domain. Together, these results demonstrate that MoRE relocated into Ncore is functionally recognized by the RdRp complex and sufficient to support all bioactivities required for the MeV RdRp transcriptase. Standard N-like bioactivity of Ncore-MoRE-Δ86 reveals that the physical separation of MoRE from its native environment, and hence from any hypothetical short-range regulatory activity that was speculatively attributed to box 3, does not impair N support of transcriptase activity.

Physical interaction of N MoRE mutants with P protein domains

Because the previously described N-Δ86 mutant lacking MoRE was bioactive in minireplicon assays but impaired in forming high-affinity interactions with the C-terminal PCT fragment of the MeV P protein harboring the MoRE-binding P-XD domain in coimmunoprecipitation experiments (*23*), we asked whether the relocation of MoRE into Ncore restores efficient interaction of N with PCT. All N mutants were subjected to a coimmunoprecipitation study using full-length P, the PCT, and the N-terminal PNT domain as targets. Ncore-MoRE coprecipitated P-Edm with an efficiency of approximately 75% that of standard N, whereas the corresponding N-noMoRE failed to appreciably precipitate P (Fig. 4A). As we previously reported, tail truncation partially restored the ability of N to interact with P in the absence of MoRE.

Coprecipitation of the PCT fragment with the Ncore-MoRE mutants essentially mirrored the results obtained for full-length P (Fig. 4B), thus demonstrating efficient interaction of the P-XD with the relocated MoRE. As observed previously, N-Δ86 without a MoRE added to Ncore did not interact appreciably with PCT, indicating that the MoRE-independent docking of P to tail-truncated N is mediated by residues in the N-terminal P fragment. Accordingly, only the two N mutants featuring the substantially truncated Δ86-tail architecture efficiently coprecipitated PNT (Fig. 4C). As expected, the N interaction with PNT, which lacks the XD domain, was not substantially affected by the presence or absence of MoRE in the different N mutants because all other N mutants did not coprecipitate PNT.

These results confirm that the relocated MoRE is recognized by and capable of engaging in high-affinity interaction with P-XD. Unstructured full-length Ntails lacking MoRE interfere with Ncore-to-P binding because both standard P and truncated PNT failed to interact with N-noMoRE (which contains the unstructured Ntail but not MoRE), but efficiently coprecipitated N-Δ86 lacking both MoRE and unstructured Ntail residues. However, only standard P, but not PNT, efficiently interacted with standard N, which naturally contains both MoRE and the unstructured Ntail. Because only the P-XD motif located in the P protein PCT domain complexes with MoRE, these data demonstrate by exclusion that the PNT region in standard P is capable of interacting with Ncore and that it is the presence of the unstructured Ntail residues that blocks this interaction in the absence of MoRE. Finally, the length of the unstructured Ntail region appears to modulate the strength of this negative effect on interaction because PNT coprecipitation efficiency was higher with tail-truncated N-Δ86 than with the longer N-Δ86-B3.

Recovery of recMeV harboring Ncore-MoRE

Minireplicon assays provide basic insight into the functionality of RdRp and N:RNA complexes, but are insufficient to determine whether all distinct bioactivity requirements for productive virus replication are met. For instance, N-Δ86 supports substantial minireplicon activity, but we were previously unable to recover MeV recombinants containing this mutant in place of standard N. To probe the full bioactivity spectrum of the Ncore-MoRE constructs, we transferred the five mutants into a complementary DNA (cDNA) copy of the MeV-Edm genome. To facilitate the detection of emerging infectious centers and potentially poorly replicating recombinants, we used a genome version that also contains an enhanced green fluorescent protein (eGFP) ORF inserted in pre-N position (*48*).

Of the five different N mutants (N-2xMoRE, Ncore-MoRE, N-noMoRE, Ncore-MoRE-Δ86, and Ncore-MoRE-Δ86-B3), recMeV-N-noMoRE virions lacking MoRE could not be recovered, which is consistent with the lack of appreciable bioactivity of the N-noMoRE mutant in the minireplicon assays (Fig. 5A). Strikingly, however, the corresponding recMeV-Ncore-MoRE recombinant featuring the relocated MoRE domain was viable and could be readily amplified, similar to standard recMeV and the recMeV-N-2xMoRE mutant with intact Ntail domain that were included as controls. In contrast, recMeV-Ncore-MoRE-Δ86 could be recovered in principle, but the recombinant appeared to be severely growth-impaired, preventing the generation of a virus stock (Fig. 5A). However, the addition of the eight-residue box 3 to the truncated Ntail was sufficient to partially restore virus growth because we successfully recovered the corresponding recMeV-Ncore-MoRE-Δ86-B3 mutant strain. Despite initial rescue at 37°C, this mutant could only be efficiently amplified at 32°C, suggesting a temperature-sensitive phenotype (Fig. 5A).

The presence of the different modifications introduced into the N ORF in recovered recMeV mutants was confirmed in all cases of successful virus amplification through RT-PCR and DNA sequencing. In addition, the electrophoretic mobility of the different N protein variants was assessed through immunoblotting of infected cell lysates (Fig. 5B). DNA sequencing did not reveal any additional point mutations that could have spontaneously occurred during virus rescue, and N mobility profiles were also consistent with that of our initial immunoblots of cells transiently transfected with expression plasmids of the different N mutants.

To assess growth kinetics of the three recMeV-Ncore-MoRE mutants that could be amplified, we generated multistep growth curves at both 37° and 32°C (Fig. 5, C and D). Maximal growth rate and peak titer of recMeV-N-2xMoRE were virtually identical to those of standard recMeV at either temperature. The recMeV-Ncore-MoRE recombinant likewise showed robust replication under both conditions, but regression modeling revealed that maximal growth rates and peak titers remained behind those of standard recMeV (Fig. 5, C and D). In

contrast, we could efficiently amplify the recMeV-Ncore-MoRE-Δ86-B3 strain only at reduced temperature (32°C), confirming temperature sensitivity of this mutant (Fig. 5D). At the permissive temperature, however, growth rates and peak titers were essentially identical to those of recMeV-Ncore-MoRE, lagging slightly behind standard recMeV.

These results indicate that RdRp must be able to engage in high-affinity interactions with N:RNA for virus viability. However, the precise physical environment of MoRE and the placement of native MoRE near the terminus of the unstructured Ntail region are not essential for fundamental activities required for successful virus replication, including loading of RdRp onto and/or RdRp progression along the N:RNA genome.

Contribution of the central, unstructured Ntail section to transcriptase processivity

Notably, of the closely related paramyxovirus and pneumovirus families, only the paramyxoviridae have elongated Ntail domains (Fig. 1B). In addition, only the paramyxoviruses cotranslationally edit P ORF transcripts to express immunomodulatory nonstructural proteins (*49*–*52*), whereas the pneumoviridae encode the equivalent proteins in separate transcription units. mRNA editing involves pausing and backsliding of the polymerase complex, which is thought to require looping out of the nascent strand before polymerization continues (*49*, *53*, *54*). The unstructured central Ntail section could provide the flexibility required for looping out of the newly synthesized strand, whereas MoRE at the end of the unstructured tail could

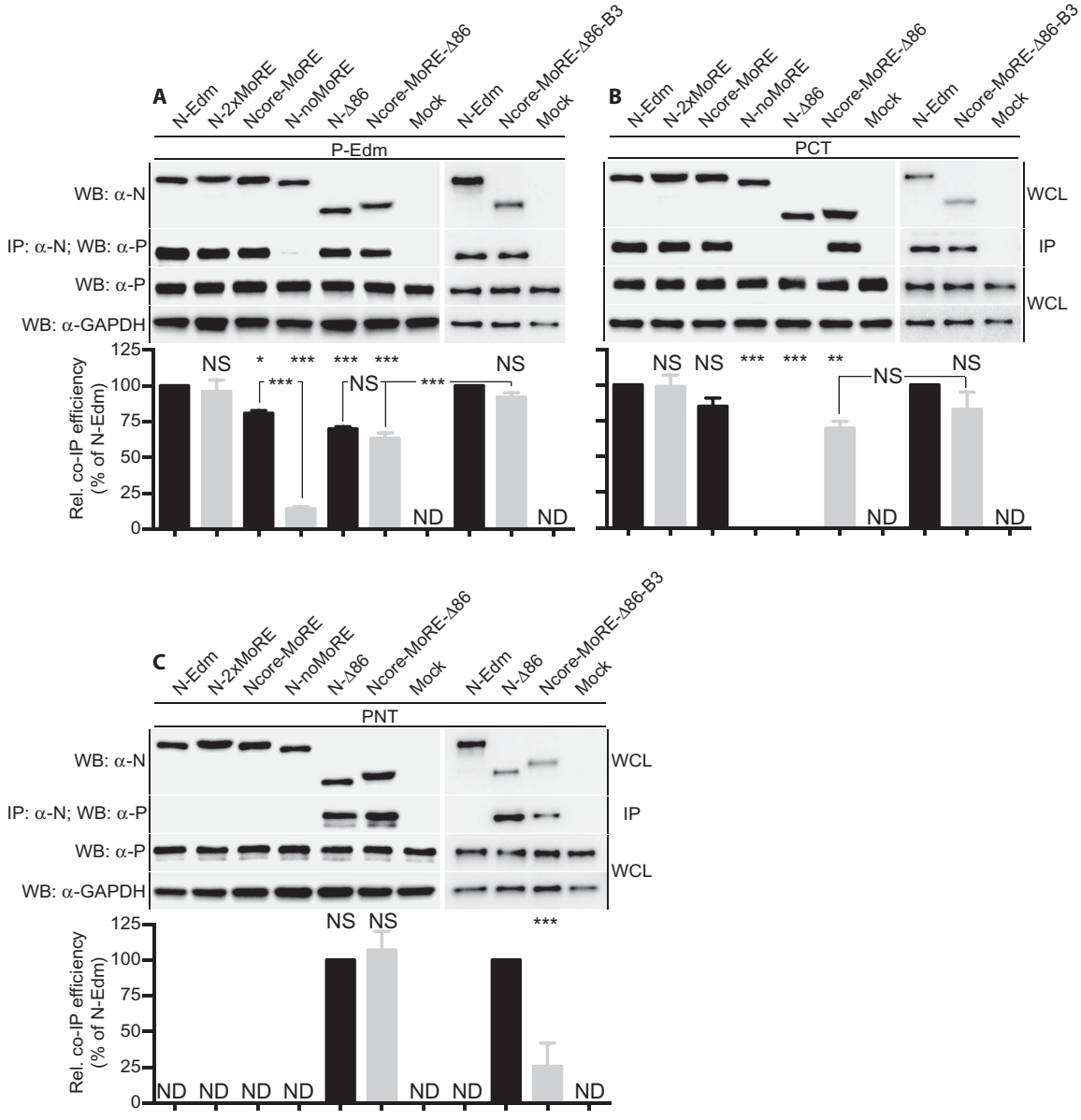

Fig. 4. Interaction of transiently expressed N protein mutants with the MeV P protein. (**A** to **C**) Coimmunoprecipitation analysis of standard MeV P protein (A) or C-terminal (B) and N-terminal (C) fragments of the MeV P protein only (PCT and PNT, respectively) with the different N constructs. Western blots (WB) of WCL and immunoprecipitation (IP) results are shown. Cellular GAPDH was detected as internal standard. Graphs depict densitometric quantitation of the relative coimmunoprecipitation efficiencies. Values represent averages of three independent experiments ± SD. Experimental variation was assessed through one-way ANOVA combined with Sidak's multiple comparison post test (*P < 0.05; **P < 0.01; ***P < 0.001; NS, not significant; ND, not determined).

simultaneously tether the paused RdRp complex to the genome, preventing catastrophic premature termination.

Consequently, we asked whether the presence of a partially unstructured Ntail followed by the MoRE interaction site is causally linked to the ability to edit mRNA. Because the growth patterns of recMeV-Ncore-MoRE and recMeV-Ncore-MoRE-Δ86-B3 at permissive temperature closely resembled each other, only the former strain was included in this experiment. Total RNA was extracted from infected cells, and cDNA reverse transcripts were subjected to next-generation sequencing to determine the relative ratio of mRNAs encoding

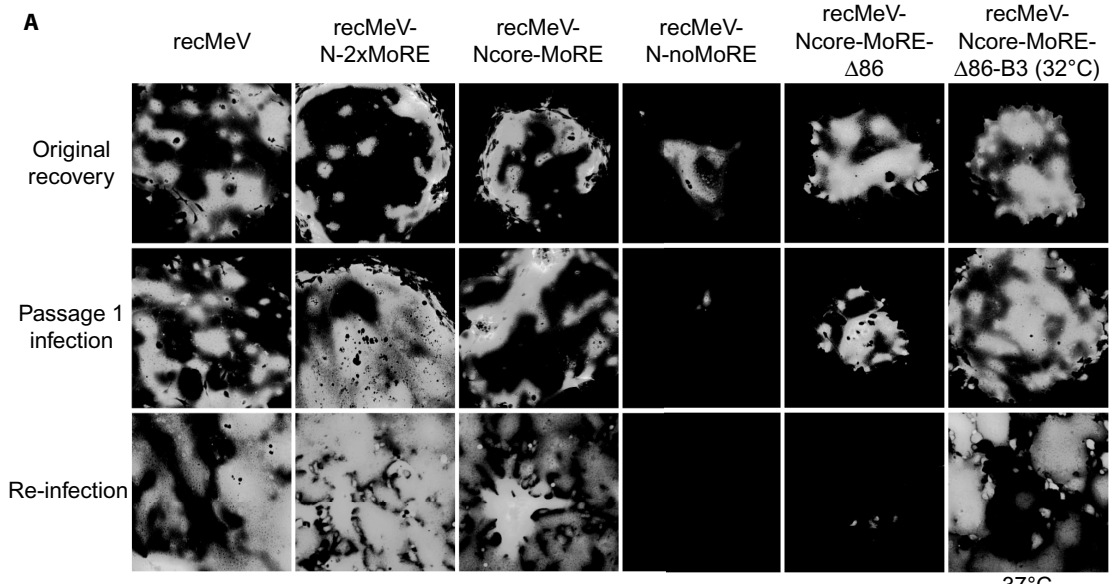

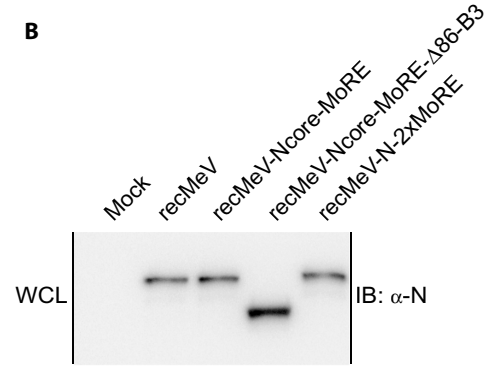

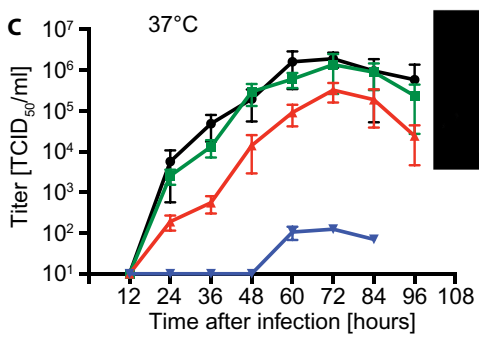

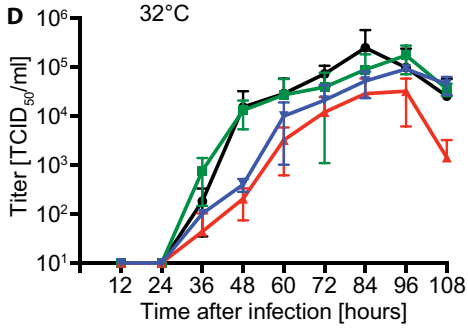

		T [°C]	PDT_{max} [hours]	$Titer_{max}$ [$TCID_{50}$/ml]
recMeV	—	37	2.0 (1.8–2.1)	1.9×10^6 (1.3×10^6–6.9×10^6)
		32	3.4 (3.2–3.9)	2.6×10^5 (1.7×10^5–3.9×10^5)
recMeV-N-2xMoRE	—	37	2.3 (2.2–2.5)*	1.1×10^6 (7.1×10^5–6.1×10^6)^{NS}
		32	3.5 (3.3–3.7)^{NS}	1.9×10^5 (1.3×10^5–3.8×10^5)^{NS}
recMeV-Ncore-MoRE	—	37	3.6 (3.5–3.8)*	3.3×10^5 (2.6×10^5–4.0×10^5)*
		32	5.9 (5.6–6.4)*	3.2×10^4 (2.2×10^4–4.9×10^4)*
recMeV-Ncore-MoRE-Δ86-B3	—	37	ND	ND
		32	5.4 (5.1–5.9)*	6.8×10^4 (5.4×10^4–8.6×10^4)*

Fig. 5. Growth profiles of recombinant MeV harboring N mutants with relocated MoRE. (**A**) Recovery of recMeV strains with modified N proteins in exchange of standard N and expressing eGFP from an additional transcription unit. Fluorescence microphotographs show cells transfected with virus recovery plasmids (Original recovery), after the first passage of infectious centers (Passage 1 infection), and after infection with cell-associated virus stocks (Re-infection). Images of fluorescent syncytia show representative fields of view. All viruses were grown at physiological temperature, with the exception of recMeV-Ncore-MoRE-Δ86-B3, which was recovered and amplified at 32°C. Cells infected with this recombinant and incubated at 37°C are shown for comparison in the bottom-most panel. (**B**) Immunoblot analysis of WCL of cells infected with the specified recMeV strains. Cells infected with recMeV-Ncore-MoRE-Δ86-B3 were incubated at 32°C. (**C** and **D**) Growth curves of the viable recMeV mutant strains in comparison with standard recMeV. Cells were infected at a multiplicity of infection (MOI) of 0.01, followed by incubation at 37°C (C) or 32°C (D), respectively. Values show titers of cell-associated progeny virus particles and represent averages of three independent repeats ± SD. For regression modeling, Bindslev's population growth four-parameter variable slope model was applied (PDT_{max}, maximal population doubling time; $Titer_{max}$, titer corresponding to the top plateau of the regression models; values in parentheses specify 95% confidence intervals; * denotes nonoverlapping 95% confidence intervals relative to standard recMeV; NS, overlapping 95% confidence intervals; ND, not determined).

MeV P, V, or W, respectively. For each virus strain examined, a minimum of 27,469 distinct reads representing five independent infection experiments were analyzed. Standard recMeV showed relative P/V/W mRNA ratios of 65%:32%:3% (Fig. 6A), which is consistent with previous estimates of the morbillivirus mRNA editing frequency (*53*). Both mutant viruses retained the ability to efficiently mRNA edit (recMeV-N-2xMoRE, 66%:31%:3%; recMeV-Ncore-MoRE, 65%:32%:3%), indicating that positional flexibility of MoRE relative to the N:RNA helix trunk is not required for the assembly of a functional mRNA editing machinery.

Therefore, we probed whether MoRE relocation and/or the presence of the unstructured central Ntail section alternatively affect the processivity of the RdRp complex moving along the N:RNA template during virus replication. The paramyxovirus replication cycle comprises primary transcription of viral mRNAs from the incoming genomes early during infection, followed by synthesis of antigenomes and progeny genomes once a sufficient level of N protein has become available for encapsidation (*55*). Whereas the viral mRNA pool expands exponentially in later replication stages, primary transcription is characterized by linear growth. To examine transcription rates, we spin-inoculated cells with recMeV-Ncore-MoRE or standard recMeV for synchronized infection and used TaqMan-based quantitation of viral N mRNA in a 30-hour window after warming of cells to 37°C (Fig. 6B). During the first 9 hours after infection, the N mRNA pools in cells infected with standard recMeV and recMeV-Ncore-MoRE increased with similar rates. Subsequently, however, standard recMeV entered the exponential mRNA expansion phase approximately 10 hours earlier than recMeV-Ncore-MoRE, resembling the virus growth profiles shown in Fig. 5C. When incubated at physiological temperature, no appreciable N mRNA pool expansion was detectable in cells infected with recMeV-Ncore-MoRE-Δ86-B3.

To appreciate viral RNA steady-state levels late in infection, we examined antigenome and N mRNA copies present in cells infected with recMeV, recMeV-Ncore-MoRE, or recMeV-Ncore-MoRE-Δ86-B3 and incubated for 72 hours at either 37°C or 32°C (recMeV and recMeV-Ncore-MoRE-Δ86-B3 only). At this stage of infection, we detected statistically significant differences in viral RNA copy numbers only in cells infected with recMeV-Ncore-MoRE-Δ86-B3 versus standard recMeV after incubation at nonpermissive temperature (Fig. 6C). Having thus verified the presence of both antigenomic and mRNA pools in this sample set, we queried the RNA panel for the viral transcription gradient by determining the relative quantities of the MeV N and L protein–encoding mRNAs, respectively, through qRT-PCR (Fig. 6D). The relative quantities of L to N mRNAs in recMeV-Ncore-MoRE–infected cells were indistinguishable from those obtained for standard recMeV. However, recMeV-Ncore-MoRE-Δ86-B3–infected cells contained significantly higher relative levels of L mRNAs compared to standard recMeV-infected cells. This relative up-regulation of L mRNA copies was independent of incubation at permissive or restrictive temperature, indicating a flattened transcription gradient experienced only by the mutant that lacks the disordered central Ntail section.

To investigate the effect of a single intergenic sequence on the transcription gradient of this mutant strain, we compared P protein versus N protein mRNA levels of the recMeV-Ncore-MoRE-Δ86-B3 mutant and standard recMeV strains (Fig. 6E). This experiment showed virtually identical P and N protein mRNA levels in recMeV-Ncore-MoRE-Δ86-B3–infected cells, but relative P mRNA levels that were approximately 15% lower than N mRNA levels in recMeV-infected cells. However, the phenotype was naturally less pronounced over a single intergenic junction than over the length of the viral genome and was therefore statistically not robust.

At each intergenic junction, paramyxovirus polymerases fail to recognize gene-end signals with low frequency and generate polycistronic mRNAs, of which the downstream ORFs cannot be accessed by the host cell ribosome and are therefore nonproductive. To test whether the flattened transcription gradient of the recMeV-Ncore-MoRE-Δ86-B3 strain reflects a higher relative amount of polycistronic mRNAs generated in cells infected by this mutant, we compared the amounts of mRNAs harboring N/P and H/L intergenic sequences relative to N protein and H protein mRNAs, respectively, in cells infected with recMeV-Ncore-MoRE-Δ86-B3 or standard recMeV (Fig. 6E). In both cases, we found a significantly higher relative amount of polycistronic mRNAs in cells infected with the mutant strain than unmodified MeV.

These findings reveal that positional flexibility of native MoRE, mediated through the unstructured central Ntail section, has not evolved to enable mRNA editing. Independent of the relative position of MoRE, the central Ntail section instead critically affects RdRp transcriptase productivity twofold: Removal of the disordered residues reduces the initial accumulation of viral RNA and improves the likelihood that the transcriptase complex, once engaged, reaches downstream ORFs. The latter appears to be achieved, at least in part, by an increased frequency of ignoring gene-end signals and generating polycistronic mRNAs in the absence of the disordered tail residues.

DISCUSSION

Recently solved N:RNA and RdRp structures and substructures have advanced the spatial understanding of the mononegavirales polymerase machinery (*10*, *16*, *20*, *22*, *25*, *26*, *56*, *57*). However, mechanistic insight, especially into the interplay between the RdRp complex and the encapsidated genomes, remains limited. This interaction is highly dynamic because the template must be locally de-encapsidated to expose the RNA to the advancing polymerase complex, followed by re-encapsidation as the polymerase progresses. N proteins of the paramyxoviruses contain, in addition to the RNA-encapsidating Ncore, a structurally mostly disordered Ntail domain proposed to have major functional importance for interaction with and advancing of RdRp (*5*, *15*, *30*, *42*, *46*). However, related mononegavirales families such as the pneumoviruses and rhabdoviruses lack equivalent unstructured tails, underscoring the fact that disordered Ntails are not a priori required to enable a mononegavirales RdRp to negotiate the N:RNA template. Understanding the functional role of the disordered Ntail regions for paramyxovirus RNA synthesis and appreciating drivers of Ntail evolution was therefore the overarching goal of this study.

Previous approaches toward this goal were hampered by the challenge that disintegration of the Ntail into discrete functional domains disrupts viral viability, preventing their functional characterization in the physiologically relevant context of virus infection (*23*, *39*). Although some recombinant viruses with individual point mutations in the conserved Ntail boxes were recovered (*39*), the insight gained from these mutants is inherently limited, and the interpretation of viral phenotypes is further complicated by the unknown contribution of cis-acting elements that are suspected to be present in Ntail (*58*, *59*). The driving force for the development of the disordered Ntail region, which comprises approximately 50% of the overall length of the tail, and its function in virus replication remained therefore unexplored. Because we had demonstrated in previous work that the presence of the RdRp-binding MoRE is required for virus viability, albeit not for

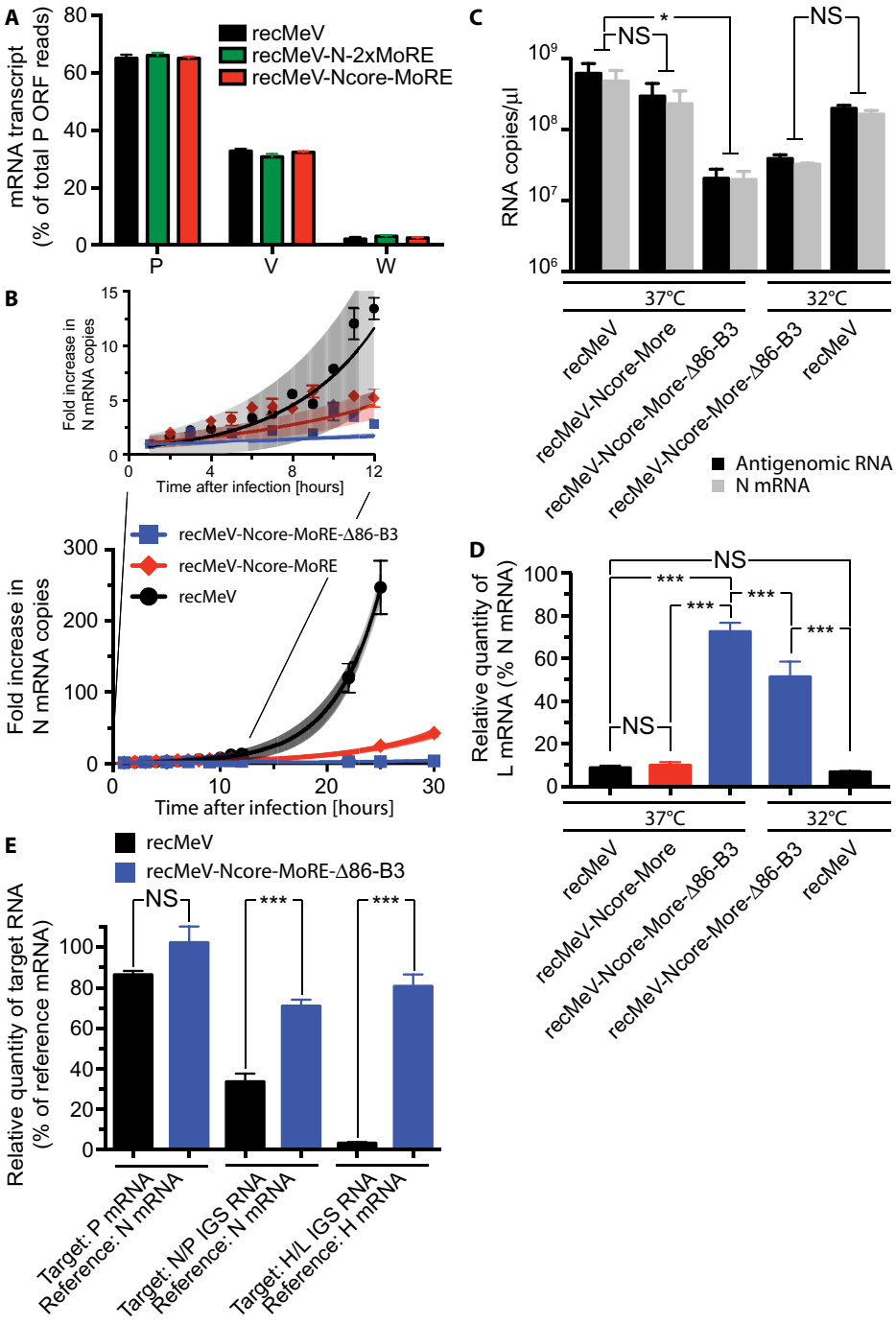

Fig. 6. Functional characterization of RdRp activity of the recMeV mutants with modified N proteins. (**A**) Next-generation sequencing analysis of P transcripts of the recMeV mutants and standard recMeV. All strains displayed identical ratios of P-, V-, and W-encoding mRNAs, indicating unchanged mRNA editing activity. Values represent a minimum of 27,469 reads each and are expressed as percentage of the differentially edited mRNAs relative to the total transcripts from the P ORF. (**B**) TaqMan-based quantitation of the N mRNA transcription rates in cells infected with standard recMeV or the specified mutant strains and incubated at 37°C. RNA extracts were normalized for 18*S* ribosomal RNA (rRNA), and N mRNA copy numbers are expressed relative to those present 1 hour after infection. The inset magnifies fold changes experienced in the initial 12-hour window after spin inoculation of cells. Values represent averages ± SEM of three independent experiments, analyzed in duplicate each. Shaded areas flanking the curves show 95% confidence intervals of the regression models. (**C**) TaqMan quantitation of MeV antigenome and N mRNA copy numbers in cells infected with standard recMeV or the specified mutant strains at 72 hours after infection. recMeV-Ncore-MoRE-Δ86-B3 was analyzed after incubation at both permissive and restrictive temperature. (**D** and **E**) qRT-PCR analyses of the RNA panel shown in (C) after first-strand synthesis using oligo(dT) primers to determine ratios of N- and L-encoding mRNAs (D), N- and P-encoding mRNAs (E), and the relative amount of intergenic sequence (IGS) containing polycistronic mRNAs relative to the IGS-preceding ORF (E). Values represent the percentage of L mRNA relative to N mRNA in each sample (D) or the percentage of the specified target mRNA relative to the specified reference mRNA (E). For (C) to (E), averages ± SEM of three independent experiments are shown, analyzed in duplicate each. Experimental variations were assessed through one-way ANOVAs combined with Sidak's multiple comparison post tests (*$P < 0.05$; ***$P < 0.001$; NS, not significant).

RdRp activity in minireplicon assays (*23*), we hypothesized that MoRE cannot be entirely removed from a viable virus, but it should be possible to physically separate the disordered Ntail region and MoRE. We further hypothesized that a high-affinity RdRp binding site may have been present in Ncore of an ancestral mononegavirales, providing the basis for our overarching assumption that it should be feasible to relocate MoRE into the Ncore of modern MeV.

A linker-scanning mutagenesis revealed only a single candidate target site for insertions in Ncore. However, suitability of this site for MoRE relocation was supported by a recent cryo-electron microscopy (cryo-EM)–based reconstruction of the MeV N:RNA in near-atomic resolution (*25*). Here, low electron density was obtained for a segment spanning residues 133 to 142, suggesting a role as interdomain linker. On the basis of the comprehensive nature of our scan and the electron density maps of assembled MeV N:RNA nucleocapsids, it is highly likely that this microdomain represents the only viable entry point for peptidic insertions in Ncore without losing N bioactivity. Structure simulations of MoRE in Ncore predicted that positional flexibility of relocated MoRE would be largely eliminated and posited the element up to 75 Å closer toward the center of the N:RNA helix. Fully consistent with these predictions, Ncore-MoRE with relocated MoRE was as bioactive in minireplicon assays as the N-2xMoRE reference construct harboring two MoRE domains and supported efficient replication of recombinant virus.

Four major mechanistic conclusions can be drawn from the characterization of the N proteins with relocated MoRE in functional assays and the context of recombinant viruses. First, high-affinity attachment points for RdRp on the N:RNA helix are essential for virus replication, albeit not for RdRp polymerase function per se, because both Ncore-MoRE and N-Δ86 were equally bioactive in minireplicon assays but only the former supported recovery and growth of recombinant virions. This finding confirms that the MoRE binding sites are not fundamentally required for the original loading of the RdRp complexes onto the N:RNA template but are necessary to prevent premature termination of the advancing RdRp complex when the template length reaches full-genome size, as we have previously shown for the N-Δ86 construct (*23*). The presence or absence of MoRE does not specifically affect the ability of the RdRp transcriptase to negotiate intergenic junctions and reinitiate mRNA synthesis, as was sometimes proposed (*30*, *42*, *59*), because the relative transcription efficiencies of the downstream reporter of both our newly generated bi- and tricistronic minigenome constructs in the presence of all bioactive N mutants including N-Δ86 were identical to those obtained with standard N.

Second, however, the position of the high-affinity contact points near the end of the flexible Ntail and downstream of the structurally disordered Ntail section is optional, rather than mechanistically required, as originally proposed (*58*–*61*). Successful recovery and amplification of both the recMeV-Ncore-MoRE and recMeV-Ncore-MoRE-Δ86-B3 recombinants demonstrate that positional flexibility of MoRE and proposed cis-acting regulatory effects (*58*–*60*) are not essential for any of the diverse activities of RdRp in virus replication. Consistent with previous studies by our group and others of short Ntail truncations eliminating native MoRE (*23*), the selective removal of only the MoRE from Ntail (as in the N-noMoRE mutant) nearly completely abolishes N bioactivity. Before our analysis of N-Δ86 (*23*), this observation formed the basis for the original model that places MoRE at the center of any productive interaction of MeV RdRp with the N:RNA nucleocapsid (*13*, *38*, *62*, *63*). In contrast to this MoRE-centric view, our data now demonstrate that it is not the absence of MoRE that prevents N-noMoRE bioactivity in minireplicon assays but rather the structurally disordered central Ntail section that has a dominant negative effect on RdRp activity. Consequently, eliminating this disordered section through truncation restored minireplicon activity (*23*), demonstrating that morbillivirus P-L can productively interact with Ncore in the absence of MoRE. Our coimmunoprecipitation studies revealing partially restored interaction of the N-terminal PNT fragment with N-Δ86 and Ncore-MoRE-Δ86 confirm this conclusion biochemically. In the presence of the disordered Ntail section, however, MoRE is required to override this dominant-negative effect, which can be achieved equally efficiently by MoRE located in Ncore as in Ntail.

Third, the presence of the conserved box 3 is mandatory for efficient virus replication, but box 3 does not directly contribute to polymerase activity: Ncore-MoRE-Δ86 was as active as standard N-Edm in minigenome assays, but only the corresponding recMeV-Ncore-MoRE-Δ86-B3 recombinant could be recovered and amplified, albeit at reduced temperature. MeV box 3 was demonstrated to interact with the viral M protein and thus be required for the interaction between viral genomes and envelope (*35*). The poor viability of recMeV-Ncore-MoRE-Δ86, which could be recovered initially but not expanded, could reflect impaired particle assembly, although recMeV lacking the M protein remain viable, albeit with a major growth phenotype (*64*). Notably, a possible contribution of Ntail to correctly position box 3 for M binding and particle assembly could also be reflected by our observation that peak progeny titers of recMeV-Ncore-MoRE-Δ86-B3 at 37°C were approximately three to four orders of magnitude lower than those of standard recMeV, whereas antigenomic RNA and N mRNA levels were reduced by only 1.5 orders of magnitude under these temperature conditions. In addition to virion assembly, box 3 has further been implicated in interacting with Hsp72 (*37*), and it could also be the disruption of this interaction or impaired contact with other host cell cofactors that prevents amplification of the recMeV-Ncore-MoRE-Δ86 recombinant.

Last, the structurally disordered central Ntail section affects the natural paramyxovirus transcription gradient of mRNA synthesis (*58*) through two synergistic effects, promoting the initiation of the transcriptase complex and reducing the success of the transcriptase to negotiate the entire genome. However, the lower tendency of premature polymerase termination in the absence of the disordered tail residues coincides with an increased frequency of generating nonproductive polycistronic mRNAs, suggesting that the central Ntail section supports the transcriptase complex in correctly processing gene-end signals, possibly by providing necessary spatial flexibility to enable the nontemplated polyadenylation of newly synthesized mRNAs. The former conclusion, promotion of the initiation of the transcriptase complex, is based on our qRT-PCR assessment of the kinetic of mRNA expression and antigenome synthesis in virus-infected cells, whereas the latter, reduction of the ability of the transcriptase to negotiate entire genomes, is substantiated by the relative quantitations of N- and L-encoding mRNA steady-state levels and mRNAs containing intergenic junctions in cells infected with recMeVNcore-MoRE (contains the disordered tail residues) and recMeV-Ncore-MoRE-Δ86-B3 (lacks the disordered tail section), respectively. Therefore, we postulate that the structurally disordered Ntail section adds a regulatory mechanism to ensure proper paramyxovirus protein expression. This modulation of the MeV transcription gradient is independent of the physical proximity of MoRE to the disordered residues but was significant only in the context of virus replication and not in our bi- and tricistronic minigenome assays. This dependence of the phenotype on virus replication could reflect the absence of the viral M protein from the minireplicon assays, given that MeV M not only may function as a particle

assembly organizer but, as recently suggested, also may be able to form tubular structures surrounding the N:RNA nucleocapsid (*65*). Although the physiological significance of these structures is unknown at present, they could impair the accessibility of the N:RNA genome by RdRp. The disordered section of the Ntails may compound the interaction of M with box 3 located at the distal end of the tail, thereby down-regulating the frequency with which these tubular M structures form, which could prevent a premature shutdown of genome access by RdRp.

At present, it cannot be definitively concluded whether the disordered Ntails represent a more recent development of the paramyxoviruses or, instead, an ancestral feature of mononegavirales N proteins. Of the modern mononegavirales, viruses of three families feature disordered domains at the N protein C terminus, whereas two families lack an Ntail domain. On the basis of our experience that the high-affinity binding site for the RdRp complex can be readily moved into paramyxovirus Ncore, we favor the view that a tailless N may represent the developmental starting point. An RdRp binding site located near the C terminus of Ncore, as seen in modern rhabdoviruses, could have enabled tail formation through the acquisition of additional residues upstream of this contact site. The emerging tails may then have provided a platform to gain novel N functionality such as a broadened repertoire of interactions with host cell factors or to expand and optimize existing functionality without compromising the essential bioactivity of the highly structured Ncore. Providing an additional regulatory mechanism for balanced viral protein expression may have been a driving force for the evolution of the unstructured Ntail region. Selective pressure on the structurally disordered central MeV Ntail section has thus likely concentrated predominantly on maintaining the length of this region rather than the actual amino acid sequence. The readiness of MeV Ntail to tolerate random short transposon insertions without loss of virus viability corroborates this view (*66*, *67*).

The presence or absence of MoRE from Ntail has no effect on the frequency of cotranslational paramyxovirus mRNA editing. We originally considered a direct link because the closely related pneumoviruses lack Ntail domains and express immunomodulatory nonstructural proteins from separate transcription units rather than through mRNA editing. Although viral countermeasures to the innate immune response are thus not directly impaired by the tail modifications, manipulating the mononegavirales transcription gradient reportedly drives virus attenuation in vivo (*68*–*71*). We therefore expect that shortening the length of the disordered Ntail section may likewise modulate viral pathogenesis. The reduced fitness of the mutant MeV recombinants analyzed in this study and, in particular, the temperature-sensitive growth phenotype of recMeV-Ncore-MoRE-Δ86-B3 support this hypothesis, which is currently tested experimentally. If our predictions are met, varying the Ntail length may constitute a novel and universal approach toward engineering next-generation attenuated recombinant vaccine strains against existing and newly emerging pathogens of the paramyxovirus family.

MATERIALS AND METHODS

Cell culture, viruses, and transfection

African green monkey kidney epithelial [CCK-81; American Type Culture Collection (ATCC)] cells stably expressing human signaling lymphocytic activation molecule (SLAM) (Vero/hSLAM) and baby hamster kidney (C-13; ATCC) cells stably expressing T7 polymerase [BSR-T7/5 (*72*)] were maintained in Dulbecco's modified Eagle's medium supplemented with 10% fetal bovine serum at 37°C and 5% CO_2. Every fifth passage, both cell lines were incubated in the presence of G-418 (100 μg/ml). Here, recMeV (*73*) and expression plasmids based on the MeV-Edm or MeV-ICB strains were used. For virus stock preparation, Vero-SLAM cells were infected at an MOI of 0.01 and incubated at 37°C, and cell-associated virus was released through two consecutive freeze/thaw cycles. Viral titers were determined by 50% tissue culture infectious dose ($TCID_{50}$) (*74*). Cells were transfected using Lipofectamine 2000 (Invitrogen) or GeneJuice (Millipore) reagents according to the manufacturer's instructions. GeneJuice was used for all virus recovery transfections.

In silico analysis of MeV N domain organization

MeDor (*75*) was used to predict disordered domains in MeV-Edm N using the IUPred (*76*), GlobPlot2 (*77*), DisEMBL (*78*), FoldIndex (*79*), SPRITZ (*80*), and RONN (*81*) algorithms. Furthermore, MeV-Edm N was submitted to PONDR-FIT (*82*) and Disopred (*83*) for disorder predictions. To quantitatively assess the consensus of all algorithms, average values of GlobPlot2, FoldIndex, and DomCut (*84*) were transformed to positive integers, and positive output scores of all algorithms were normalized for identical hit cutoff values. All average scores were then transformed to a scale of 0 to 10 and plotted as a function of MeV-Edm N residues. MeV-Edm N secondary structure prediction was based on the StrBioLib library of the Pred2ary program (*85*), embedded in the MeDor package (*75*). For the identification of disordered regions in MeV-Edm N based on DomCut (*84*), paramyxovirus N protein sequences were aligned using the ClustalW2 (*86*) and MUSCLE (*87*) algorithm. Results of three different settings were compared, and relative DomCut propensity scores were then averaged separately on the basis of the different sequence alignments: (i) different MeV genotypes [MeV-Edm (genotype A) (AF266290.1), MeV-Gambia (genotype B2) (EU332919.1), MeV-Toulon (genotype C2) (HM562906.1), MeV-Amsterdam (genotype G2) (EU090818.1), MeV-Illinois (genotype D3) (EU139098.1), MeV-Alaska (genotype H2) (AY037043.1)], (ii) different morbilliviruses [MeV-Edm, MeV Gambia B2, MeV-Toulon, MeV-Alaska, MeV Amsterdam, RPV-KabeteO (X98291.3), CDV Onderstepoort (AF378705.1), CDV 5804 (AY386315.1), peste des petits ruminants virus Turkey 2000 (NC_006383.2), dolphin morbillivirus (NC_005283.1)], and (iii) members of all paramyxovirus genera [MeV-Edm, CDV 5804, NIV (NC_002728.1), HPIV type 1 C35 (NC_003461.1), HPIV type 3 LZ22 (NC_001796.2), HPIV type 2 (NC_003443.1), HPIV type 4 SKPIV4 (NC_021928.1), NDV-ISG0210 (GenBank JF340367), Tupaia paramyxovirus (NC_002199.1), RSV A2 (NC_001803.1), human metapneumovirus Sabana (NC_004148.2)].

Disorder and secondary structure prediction was performed using the MeDor package. The IUPred and FoldIndex algorithms were used for disorder prediction. Sequences used were as follows: RSV (accession: P03418.1), HMPV (accession: AAS22074.1), RABV (accession: ABN11331.1), MeV ICB strain (accession: NP_056918.1), MeV Edmonston strain (accession: BAB60956.1), CDV 5804 strain (accession: AAQ96303.1), Nipah virus (accession: AEZ01372.1), Hendra virus (accession: NP_047106.1), Sendai virus (accession: Q07097.1), Mumps strain 88-1961 (accession: AAL76262.1), VSV Indiana strain (accession: ACK77580.1), Marburg virus (MARG) (accession: YP_001531153.1), BDV (accession: 1N93_X), Ebola virus (EBOV) (accession: AIO11747.1), and Newcastle disease virus (NDV) (accession: ALR96387.1). Multiple sequence alignments and phylogenetic analysis were conducted using the Clustal Omega and ClustalW2, respectively, using

the neighbor-joining method and unweighted pair group method with arithmetic mean (UPGMA).

Computational modeling of MeV N:RNA with relocated MoREs

Homology models for MeV N:RNA with MoRE relocated to Ncore were obtained using the SWISS-MODEL homology modeling server (*47*) using the previously published MeV N:RNA structure (PDB ID: 4UFT) as a template. Images were manipulated and created using PyMOL (*88*).

Molecular biology

For N domain screening, 4–amino acid (GDAS) linker insertion constructs were cloned with appropriate primers introducing a silent Nsi I restriction site according to QuikChange protocol (Stratagene). Constructs were sequence-confirmed, and the presence of the Nsi I restriction site was confirmed. For detection purposes, those constructs were tagged with a HA tag (SGGGYPYDVPDYA) at the C terminus of N through PCR amplification using appropriate primer and religation using a silent Nde I restriction site in the tag sequence. The same strategy was applied to introduce the HA tag flanked by a short linker sequence (SGGGYPYDVPDYAGGGS) at various positions in the N protein. The MoRE domain with altered codon usage to native MoRE was inserted at residue 138 of the MeV-Edm N ORF. PCR was performed with primers containing overhanging sequences encoding for MoRE and terminal Nhe I sites for relegation. PCR mutagenesis was then performed to remove the Nhe I site. All newly generated constructs were sequence-confirmed. The MeV bicistronic replicon was first cloned into a pCR2.1-TOPO vector with the help of Aat II and Avr II sites by recombineering PCR, creating a firefly luciferase–(P/M-IGS)–nanoluciferase cassette. This construct was then cloned into an existing monocistronic MeV minigenome (*44*) with the help of Pac I and Avr II sites. The resulting bicistronic minigenome thus features the P/M-IGS between the firefly luciferase and nanoluciferase ORFs. This minigenome further served as a backbone for the tricistronic variant. A second intergenic junction cassette featuring the N/P-IGS and P ORF was generated using recombineering PCR and cloned into the bicistronic backbone with the help of Pac I and Aat II sites. To avoid the expression of functional P protein from the central ORF, a tandem stop codon was inserted into the P reading frame 21 triplets downstream of the start codon. Thus, the final construct featured a tricistronic minigenome consisting of firefly luciferase–(P/N-IGS)–P_stopstop–(P/M-IGS)–nanoluciferase.

Minireplicon luciferase reporter assay

BSR-T7/5 cells (4×10^5 per well in a 12-well plate format) were transfected with plasmids encoding for L-Edm (1.1 μg), P-Edm (0.27 μg), N-Edm and N-Edm mutant variants (0.42 μg), and the MeV luciferase replicon reporter (1.2 μg). Minireplicon assays including Ncore-MoRE constructs were carried out in 96-well plates in dependent nonuplets for increased stringency. BSR-T7/5 cells (1×10^4 per well in a 96-well plate format) were transfected with L-Edm (0.02 μg), P-Edm (0.02 μg), N-Edm and N-Edm mutant variants (0.016 μg), and the MeV luciferase replicon reporter (0.044 μg) using GeneJuice transfection reagent. Cells were lysed 40 hours after transfection in Glo lysis buffer (Promega), and luciferase activities in cleared lysates were determined using Bright-Glo luciferase substrate (Promega) in a Synergy H1 microplate reader (BioTek). To develop assays in 96-well plate format, Bright-Glo substrate was directly added to the cells, and bioluminescence was quantified after 3-min incubation for signal stabilization. Relative RdRp activities (relA) were determined on the basis of the formula % relA = (experimental − $\text{signal}_{\text{min}}$)/($\text{signal}_{\text{max}}$ − $\text{signal}_{\text{min}}$) × 100, with $\text{signal}_{\text{max}}$ corresponding to cells transfected with plasmids encoding the standard MeV-Edm proteins and $\text{signal}_{\text{min}}$ representing cells that received equal amounts of empty vector (pUC-19) in place of the N-encoding plasmid.

Antibodies, SDS-PAGE, and immunoblotting

BSR-T7/5 cells were transfected in a 12-well plate format (4×10^5 per well) with 2 μg of N-encoding plasmid DNA, and 40 hours after transfection, cells were washed once with phosphate-buffered saline (PBS) and lysed in radioimmunoprecipitation assay buffer [1% sodium deoxycholate, 1% NP-40, 150 mM NaCl, 50 mM tris-Cl (pH 7.2), 10 mM EDTA, 50 mM NaF, 0.05% SDS, protease inhibitors (Roche), 1 mM phenylmethylsulfonyl fluoride]. Cleared lysates (20,000*g*, 10 min, 4°C) were mixed with 5× urea buffer [200 mM tris (pH 6.8), 8 M urea, 5% SDS, 0.1 mM EDTA, 0.03% bromphenol blue, 1.5% dithiothreitol]. Samples were denatured for 30 min at 50°C, fractionated on 8% SDS–polyacrylamide gel electrophoresis (PAGE) gels, blotted on polyvinylidene difluoride membranes (Millipore), and subjected to enhanced chemiluminescence detection (Pierce) using specific antibodies directed against MeV-N (83KKKII, Millipore), MeV-P (9H4, Abcam), GAPDH (6C5, Ambion), α-FLAG-M2-HRP (Sigma-Aldrich), or HA (16B12, Sigma-Aldrich), as specified. Immunoblots were developed using a ChemiDoc digital imaging system (Bio-Rad). Only nonsaturated images were used for densitometry and carried out using the Image Lab package (Bio-Rad) and global background correction.

Coimmunoprecipitation

BSR-T7/5 cells (8×10^5 per well in a six-well plate format) were transfected with 2 μg each of plasmid DNA encoding a MeV N construct and either MeV Pfull, PNT_{FLAG} with a C-terminal FLAG tag, or MeV PCT_{FLAG} with an N-terminal FLAG tag. After 36 hours, cells were harvested and subjected to coimmunoprecipitation, as previously described (*6*). Following immunoprecipitation using an α-N antibody, samples were fractionated on 10% SDS-PAGE gels, followed by immunoblotting and chemiluminescence detection, as described.

Virus recovery

Recombinant MeV was recovered in BSR-T7/5 cells by transfecting 5 μg of the cDNA copy of the modified genome and ICB-N (0.8 μg), ICB-P (0.6 μg), and ICB-L (0.55 μg) using GeneJuice transfection reagent. Cells were overlaid 48 hours after transfection onto Vero/hSLAM cells, and emerging infectious particles were passaged twice in Vero/hSLAM cells. Integrity of newly rescued virus was confirmed by extracting total RNA from virus-infected cells (RNeasy Mini kit, Qiagen), and cDNA was created using random hexamer primers and SuperScript III reverse transcriptase (Invitrogen). Modified genome regions were amplified using appropriate primers and sequenced.

Multistep growth curves

Before infection for the multistep growth curve, viral stocks were diluted to approximately 1×10^4 TCID_{50}/ml, and titers were reconfirmed by TCID_{50} titration. Vero/hSLAM cells (1×10^5 per well in a 12-well format) were infected with the different MeV variants at an MOI of 0.01 TCID_{50} per well for 1 hour, and the inoculum was replaced with growth medium. Every 12 hours, samples were harvested, cell-associated virions were released through two consecutive freeze/thaw cycles, and progeny virus titers were determined through TCID_{50} titration.

Next-generation sequencing

Next-generation sequencing using MiSeq (Illumina) was performed to determine the ratio of P/V/W transcripts in recMeV constructs. When cytopathic effect (CPE) reached approximately 75 to 90%, total RNA was isolated from infected cells using the RNeasy kit (Qiagen), and cDNAs of mRNA transcripts were synthesized using oligo(dT) primers and SuperScript III reverse transcriptase (Invitrogen). MiSeq primers with Illumina overhangs targeting a region of ~500 nucleotides surrounding the P gene–editing site were used to PCR amplify cDNAs representing all P, V, and W transcripts. Next-generation sequencing was performed by the Emory Integrated Genomics Core. Sequences were queried for the relative ratios of P, V, and W transcripts for each sample.

Determination of N-L transcription gradient

To determine mRNA ratios of cell-associated virus, Vero/hSLAM cells were infected with an MOI of 0.05 for all recombinant viruses. When CPE reached approximately 75 to 90%, total RNA was isolated, as previously described, and cDNAs were synthesized using oligo(dT) primers and SuperScript RT III reverse transcriptase. The mRNA ratios were determined using appropriate primer pairs annealing in the N, L, and GAPDH ORFs and PowerUp SYBR Green Master Mix (Thermo Fisher Scientific) using an Applied Biosystems 7500 Real-Time PCR system.

Quantitation of mRNA and antigenome copy numbers

To monitor mRNA and genome amplification in a one-step replication curve, Vero-SLAM cells were infected with an MOI of 0.2 and spin-inoculated (2000*g*, 30 min, 4°C). For mRNA and genome amplification, total RNA was harvested hourly. To quantify mRNA copy numbers, oligo(dT)-primed cDNAs were synthesized, whereas for antigenome copy numbers, a specific primer located in the viral trailer sequence was used. qPCR was performed in the Applied Biosystems 7500 Real-Time PCR System using StepOnePlus Real-Time PCR System, TaqMan Fast Virus 1-Step Master Mix (Thermo Fisher Scientific), and specific primer pair 3 (*89*). To calculate RNA copy numbers, a standard curve was created using a pTM1-Edm N plasmid of known concentration and linearized with Bam HI as template. Samples were normalized on the basis of 18*S* rRNA using a Eukaryotic 18S rRNA Endogenous Control kit (Thermo Fisher Scientific).

Statistical analysis

To assess the statistical significance of differences between sample means, one-way ANOVA with Sidak's multiple comparison post tests was applied using the Prism 7 software package (GraphPad). Bindslev's population growth four-parameter variable slope model and an exponential growth model were applied for regression modeling of virus growth and RNA accumulation rates, respectively. Experimental uncertainties are depicted as SD or SEM, as specified in the figure legends.

REFERENCES AND NOTES

1. R. A. Lamb, D. Kolakofsky, Paramyxoviridae: The viruses and their replication, in *Fields Virology*, D. M. Knipe, P. M. Howley, D. E. Griffin, R. A. Lamb, M. A. Martin, B. Roizman, S. E. Straus, Eds. (Lippincott Williams & Wilkins, ed. 4, 2001), pp. 1305–1340.
2. G. Enders, in *Medical Microbiology,* S. Baron, Ed. (The University of Texas Medical Branch at Galveston, 1996).
3. M. H. Heggeness, A. Scheid, P. W. Choppin, Conformation of the helical nucleocapsids of paramyxoviruses and vesicular stomatitis virus: Reversible coiling and uncoiling induced by changes in salt concentration. *Proc. Natl. Acad. Sci. U.S.A.* **77**, 2631–2635 (1980).
4. J. T. Finch, A. J. Gibbs, Observations on the structure of the nucleocapsids of some paramyxoviruses. *J. Gen. Virol.* **6**, 141–150 (1970).
5. S. Longhi, Nucleocapsid structure and function. *Curr. Top. Microbiol. Immunol.* **329**, 103–128 (2009).
6. M. Dochow, S. A. Krumm, J. E. Crowe Jr., M. L. Moore, R. K. Plemper, Independent structural domains in the *Paramyxovirus* polymerase protein. *J. Biol. Chem.* **287**, 6878–6891 (2012).
7. S. M. Perlman, A. S. Huang, RNA synthesis of vesicular stomatitis virus. V. Interactions between transcription and replication. *J. Virol.* **12**, 1395–1400 (1973).
8. R. Fearns, M. E. Peeples, P. L. Collins, Increased expression of the N protein of respiratory syncytial virus stimulates minigenome replication but does not alter the balance between the synthesis of mRNA and antigenome. *Virology* **236**, 188–201 (1997).
9. J. Curran, D. Kolakofsky, Replication of paramyxoviruses. *Adv. Virus Res.* **54**, 403–422 (1999).
10. G. Communie, J. Habchi, F. Yabukarski, D. Blocquel, R. Schneider, N. Tarbouriech, N. Papageorgiou, R. W. H. Ruigrok, M. Jamin, M. R. Jensen, S. Longhi, M. Blackledge, Atomic resolution description of the interaction between the nucleoprotein and phosphoprotein of Hendra virus. *PLOS Pathog.* **9**, e1003631 (2013).
11. R. L. Kingston, L. S. Gay, W. S. Baase, B. W. Matthews, Structure of the nucleocapsid-binding domain from the mumps virus polymerase; an example of protein folding induced by crystallization. *J. Mol. Biol.* **379**, 719–731 (2008).
12. R. L. Kingston, W. A. Baase, L. S. Gay, Characterization of nucleocapsid binding by the measles virus and mumps virus phosphoproteins. *J. Virol.* **78**, 8630–8640 (2004).
13. R. L. Kingston, D. J. Hamel, L. S. Gay, F. W. Dahlquist, B. W. Matthews, Structural basis for the attachment of a paramyxoviral polymerase to its template. *Proc. Natl. Acad. Sci. U.S.A.* **101**, 8301–8306 (2004).
14. S. Longhi, The measles virus N_{TAIL}-XD complex: An illustrative example of fuzziness. *Adv. Exp. Med. Biol.* **725**, 126–141 (2012).
15. J. Habchi, S. Blangy, L. Mamelli, M. R. Jensen, M. Blackledge, H. Darbon, M. Oglesbee, Y. Shu, S. Longhi, Characterization of the interactions between the nucleoprotein and the phosphoprotein of *Henipavirus*. *J. Biol. Chem.* **286**, 13583–13602 (2011).
16. R. Cox, A. Pickar, S. Qiu, J. Tsao, C. Rodenburg, T. Dokland, A. Elson, B. He, M. Luo, Structural studies on the authentic mumps virus nucleocapsid showing uncoiling by the phosphoprotein. *Proc. Natl. Acad. Sci. U.S.A.* **111**, 15208–15213 (2014).
17. M. Mavrakis, S. Méhouas, E. Réal, F. Iseni, D. Blondel, N. Tordo, R. W. H. Ruigrok, Rabies virus chaperone: Identification of the phosphoprotein peptide that keeps nucleoprotein soluble and free from non-specific RNA. *Virology* **349**, 422–429 (2006).
18. M. Chen, T. Ogino, A. K. Banerjee, Interaction of vesicular stomatitis virus P and N proteins: Identification of two overlapping domains at the N terminus of P that are involved in N^0-P complex formation and encapsidation of viral genome RNA. *J. Virol.* **81**, 13478–13485 (2007).
19. F. Yabukarski, P. Lawrence, N. Tarbouriech, J.-M. Bourhis, E. Delaforge, M. R. Jensen, R. W. H. Ruigrok, M. Blackledge, V. Volchkov, M. Jamin, Structure of Nipah virus unassembled nucleoprotein in complex with its viral chaperone. *Nat. Struct. Mol. Biol.* **21**, 754–759 (2014).
20. S. G. Guryanov, L. Liljeroos, P. Kasaragod, T. Kajander, S. J. Butcher, Crystal structure of the measles virus nucleoprotein core in complex with an N-terminal region of phosphoprotein. *J. Virol.* **90**, 2849–2857 (2016).
21. C. Bernard, S. Gely, J.-M. Bourhis, X. Morelli, S. Longhi, H. Darbon, Interaction between the C-terminal domains of N and P proteins of measles virus investigated by NMR. *FEBS Lett.* **583**, 1084–1089 (2009).
22. R. Cox, T. J. Green, S. Purushotham, C. Deivanayagam, G. J. Bedwell, P. E. Prevelige, M. Luo, Structural and functional characterization of the mumps virus phosphoprotein. *J. Virol.* **87**, 7558–7568 (2013).
23. S. A. Krumm, M. Takeda, R. K. Plemper, The measles virus nucleocapsid protein tail domain is dispensable for viral polymerase recruitment and activity. *J. Biol. Chem.* **288**, 29943–29953 (2013).
24. M. Colombo, J.-M. Bourhis, C. Chamontin, C. Soriano, S. Villet, S. Costanzo, M. Couturier, V. Belle, A. Fournel, H. Darbon, D. Gerlier, S. Longhi, The interaction between the measles virus nucleoprotein and the Interferon Regulator Factor 3 relies on a specific cellular environment. *Virol. J.* **6**, 59 (2009).
25. I. Gutsche, A. Desfosses, G. Effantin, W. L. Ling, M. Haupt, R. W. H. Ruigrok, C. Sachse, G. Schoehn, Near-atomic cryo-EM structure of the helical measles virus nucleocapsid. *Science* **348**, 704–707 (2015).
26. M. Alayyoubi, G. P. Leser, C. A. Kors, R. A. Lamb, Structure of the paramyxovirus parainfluenza virus 5 nucleoprotein–RNA complex. *Proc. Natl. Acad. Sci. U.S.A.* **112**, E1792–E1799 (2015).
27. K. Johansson, J.-M. Bourhis, V. Campanacci, C. Cambillau, B. Canard, S. Longhi, Crystal structure of the measles virus phosphoprotein domain responsible for the induced folding of the C-terminal domain of the nucleoprotein. *J. Biol. Chem.* **278**, 44567–44573 (2003).

28. G. Communie, R. W. H. Ruigrok, M. R. Jensen, M. Blackledge, Intrinsically disordered proteins implicated in paramyxoviral replication machinery. *Curr. Opin. Virol.* **5**, 72–81 (2014).
29. J. Habchi, S. Longhi, Structural disorder within paramyxovirus nucleoproteins and phosphoproteins. *Mol. Biosyst.* **8**, 69–81 (2012).
30. M. R. Jensen, G. Communie, E. A. Ribeiro Jr., N. Martinez, A. Desfosses, L. Salmon, L. Mollica, F. Gabel, M. Jamin, S. Longhi, R. W. H. Ruigrok, M. Blackledge, Intrinsic disorder in measles virus nucleocapsids. *Proc. Natl. Acad. Sci. U.S.A.* **108**, 9839–9844 (2011).
31. G. Schoehn, M. Mavrakis, A. Albertini, R. Wade, A. Hoenger, R. W. H. Ruigrok, The 12 Å structure of trypsin-treated measles virus N–RNA. *J. Mol. Biol.* **339**, 301–312 (2004).
32. A. Diallo, T. Barrett, M. Barbron, G. Meyer, P. C. Lefèvre, Cloning of the nucleocapsid protein gene of peste-des-petits-ruminants virus: Relationship to other morbilliviruses. *J. Gen. Virol.* **75**, 233–237 (1994).
33. D. Laine, J. M. Bourhis, S. Longhi, M. Flacher, L. Cassard, B. Canard, C. Sautès-Fridman, C. Rabourdin-Combe, H. Valentin, Measles virus nucleoprotein induces cell-proliferation arrest and apoptosis through N_{TAIL}–NR and N_{CORE}–FcγRIIB1 interactions, respectively. *J. Gen. Virol.* **86**, 1771–1784 (2005).
34. D. Laine, M.-C. Trescol-Biémont, S. Longhi, G. Libeau, J. C. Marie, P.-O. Vidalain, O. Azocar, A. Diallo, B. Canard, C. Rabourdin-Combe, H. Valentin, Measles virus (MV) nucleoprotein binds to a novel cell surface receptor distinct from FcγRII via its C-terminal domain: Role in MV-induced immunosuppression. *J. Virol.* **77**, 11332–11346 (2003).
35. G. Ray, P. T. Schmitt, A. P. Schmitt, C-terminal DxD-containing sequences within paramyxovirus nucleocapsid proteins determine matrix protein compatibility and can direct foreign proteins into budding particles. *J. Virol.* **90**, 3650–3660 (2016).
36. M. Iwasaki, M. Takeda, Y. Shirogane, Y. Nakatsu, T. Nakamura, Y. Yanagi, The matrix protein of measles virus regulates viral RNA synthesis and assembly by interacting with the nucleocapsid protein. *J. Virol.* **83**, 10374–10383 (2009).
37. X. Zhang, J.-M. Bourhis, S. Longhi, T. Carsillo, M. Buccellato, B. Morin, B. Canard, M. Oglesbee, Hsp72 recognizes a P binding motif in the measles virus N protein C-terminus. *Virology* **337**, 162–174 (2005).
38. X. Zhang, C. Glendening, H. Linke, C. L. Parks, C. Brooks, S. A. Udem, M. Oglesbee, Identification and characterization of a regulatory domain on the carboxyl terminus of the measles virus nucleocapsid protein. *J. Virol.* **76**, 8737–8746 (2002).
39. Y. Shu, J. Habchi, S. Costanzo, A. Padilla, J. Brunel, D. Gerlier, M. Oglesbee, S. Longhi, Plasticity in structural and functional interactions between the phosphoprotein and nucleoprotein of measles virus. *J. Biol. Chem.* **287**, 11951–11967 (2012).
40. Y. Wang, X. Chu, S. Longhi, P. Roche, W. Han, E. Wang, J. Wang, Multiscaled exploration of coupled folding and binding of an intrinsically disordered molecular recognition element in measles virus nucleoprotein. *Proc. Natl. Acad. Sci. U.S.A.* **110**, E3743–E3752 (2013).
41. A. Sugai, H. Sato, M. Yoneda, C. Kai, Phosphorylation of measles virus nucleoprotein affects viral growth by changing gene expression and genomic RNA stability. *J. Virol.* **87**, 11684–11692 (2013).
42. J.-M. Bourhis, B. Canard, S. Longhi, Structural disorder within the replicative complex of measles virus: Functional implications. *Virology* **344**, 94–110 (2006).
43. F. Ferron, S. Longhi, B. Canard, D. Karlin, A practical overview of protein disorder prediction methods. *Proteins* **65**, 1–14 (2006).
44. S. A. Krumm, J. M. Ndungu, J.-J. Yoon, M. Dochow, A. Sun, M. Natchus, J. P. Snyder, R. K. Plemper, Potent host-directed small-molecule inhibitors of myxovirus RNA-dependent RNA-polymerases. *PLOS ONE* **6**, e20069 (2011).
45. D. Blocquel, J. Habchi, A. Gruet, S. Blangy, S. Longhi, Compaction and binding properties of the intrinsically disordered C-terminal domain of *Henipavirus* nucleoprotein as unveiled by deletion studies. *Mol. Biosyst.* **8**, 392–410 (2012).
46. S. Longhi, V. Receveur-Bréchot, D. Karlin, K. Johansson, H. Darbon, D. Bhella, R. Yeo, S. Finet, B. Canard, The C-terminal domain of the measles virus nucleoprotein is intrinsically disordered and folds upon binding to the C-terminal moiety of the phosphoprotein. *J. Biol. Chem.* **278**, 18638–18648 (2003).
47. M. Biasini, S. Bienert, A. Waterhouse, K. Arnold, G. Studer, T. Schmidt, F. Kiefer, T. Gallo Cassarino, M. Bertoni, L. Bordoli, T. Schwede, SWISS-MODEL: Modelling protein tertiary and quaternary structure using evolutionary information. *Nucleic Acids Res.* **42**, W252–W258 (2014).
48. W. P. Duprex, S. McQuaid, L. Hangartner, M. A. Billeter, B. K. Rima, Observation of measles virus cell-to-cell spread in astrocytoma cells by using a green fluorescent protein-expressing recombinant virus. *J. Virol.* **73**, 9568–9575 (1999).
49. D. Kolakofsky, L. Roux, D. Garcin, R. W. H. Ruigrok, Paramyxovirus mRNA editing, the "rule of six" and error catastrophe: A hypothesis. *J. Gen. Virol.* **86**, 1869–1877 (2005).
50. S. Hausmann, J. Jacques, D. Kolakofsky, Paramyxovirus RNA editing and the requirement for hexamer genome length. *RNA* **2**, 1033–1045 (1996).
51. J. P. Jacques, S. Hausmann, D. Kolakofsky, Paramyxovirus mRNA editing leads to G deletions as well as insertions. *EMBO J.* **13**, 5496–5503 (1994).
52. S. Vidal, J. Curran, D. Kolakofsky, Editing of the Sendai virus P/C mRNA by G insertion occurs during mRNA synthesis via a virus-encoded activity. *J. Virol.* **64**, 239–246 (1990).
53. D. Kolakofsky, Paramyxovirus RNA synthesis, mRNA editing, and genome hexamer phase: A review. *Virology* **498**, 94–98 (2016).
54. D. Kolakofsky, P. Le Mercier, F. Iseni, D. Garcin, Viral RNA polymerase scanning and the gymnastics of Sendai virus RNA synthesis. *Virology* **318**, 463–473 (2004).
55. S. Plumet, W. P. Duprex, D. Gerlier, Dynamics of viral RNA synthesis during measles virus infection. *J. Virol.* **79**, 6900–6908 (2005).
56. S. G. Guryanov, L. Liljeroos, P. Kasaragod, T. Kajander, S. J. Butcher, Crystal structure of the measles virus nucleoprotein core in complex with an N-terminal region of phosphoprotein. *J. Virol.* **90**, 2849–2857 (2015).
57. J. F. Bruhn, K. C. Barnett, J. Bibby, J. M. H. Thomas, R. M. Keegan, D. J. Rigden, Z. A. Bornholdt, E. O. Saphire, Crystal structure of the Nipah virus phosphoprotein tetramerization domain. *J. Virol.* **88**, 758–762 (2014).
58. J. Brunel, D. Chopy, M. Dosnon, L.-M. Bloyet, P. Devaux, E. Urzua, R. Cattaneo, S. Longhi, D. Gerlier, Sequence of events in measles virus replication: Role of phosphoprotein-nucleocapsid interactions. *J. Virol.* **88**, 10851–10863 (2014).
59. J. Habchi, S. Longhi, Structural disorder within paramyxoviral nucleoproteins and phosphoproteins in their free and bound forms: From predictions to experimental assessment. *Int. J. Mol. Sci.* **16**, 15688–15726 (2015).
60. A. Kavalenka, I. Urbančič, V. Belle, S. Rouger, S. Costanzo, S. Kure, A. Fournel, S. Longhi, B. Guigliarelli, J. Strancar, Conformational analysis of the partially disordered measles virus N_{TAIL}-XD complex by SDSL EPR spectroscopy. *Biophys. J.* **98**, 1055–1064 (2010).
61. K. Yegambaram, R. L. Kingston, The feet of the measles virus polymerase bind the viral nucleocapsid protein at a single site. *Protein Sci.* **19**, 893–899 (2010).
62. J.-M. Bourhis, K. Johansson, V. Receveur-Bréchot, C. J. Oldfield, K. A. Dunker, B. Canard, S. Longhi, The C-terminal domain of measles virus nucleoprotein belongs to the class of intrinsically disordered proteins that fold upon binding to their physiological partner. *Virus Res.* **99**, 157–167 (2004).
63. J. Curran, H. Homann, C. Buchholz, S. Rochat, W. Neubert, D. Kolakofsky, The hypervariable C-terminal tail of the Sendai paramyxovirus nucleocapsid protein is required for template function but not for RNA encapsidation. *J. Virol.* **67**, 4358–4364 (1993).
64. T. Cathomen, B. Mrkic, D. Spehner, R. Drillien, R. Naef, J. Pavlovic, A. Aguzzi, M. A. Billeter, R. Cattaneo, A matrix-less measles virus is infectious and elicits extensive cell fusion: Consequences for propagation in the brain. *EMBO J.* **17**, 3899–3908 (1998).
65. L. Liljeroos, J. T. Huiskonen, A. Ora, P. Susi, S. J. Butcher, Electron cryotomography of measles virus reveals how matrix protein coats the ribonucleocapsid within intact virions. *Proc. Natl. Acad. Sci. U.S.A.* **108**, 18085–18090 (2011).
66. S. M. Beaty, B. Lee, Constraints on the genetic and antigenic variability of measles virus. *Viruses* **8**, 109 (2016).
67. B. O. Fulton, D. Sachs, S. M. Beaty, S. T. Won, B. Lee, P. Palese, N. S. Heaton, Mutational analysis of measles virus suggests constraints on antigenic variation of the glycoproteins. *Cell Rep.* **11**, 1331–1338 (2015).
68. S. Finke, J. H. Cox, K.-K. Conzelmann, Differential transcription attenuation of rabies virus genes by intergenic regions: Generation of recombinant viruses overexpressing the polymerase gene. *J. Virol.* **74**, 7261–7269 (2000).
69. E. N. Hodges, B. S. Heinrich, J. H. Connor, A vesiculovirus showing a steepened transcription gradient and dominant *trans*-repression of virus transcription. *J. Virol.* **86**, 8884–8889 (2012).
70. D. E. Anderson, V. von Messling, Region between the canine distemper virus M and F genes modulates virulence by controlling fusion protein expression. *J. Virol.* **82**, 10510–10518 (2008).
71. D. E. Anderson, A. Castan, M. Bisaillon, V. von Messling, Elements in the canine distemper virus M 3′ UTR contribute to control of replication efficiency and virulence. *PLOS ONE* **7**, e31561 (2012).
72. U. J. Buchholz, S. Finke, K.-K. Conzelmann, Generation of bovine respiratory syncytial virus (BRSV) from cDNA: BRSV NS2 is not essential for virus replication in tissue culture, and the human RSV leader region acts as a functional BRSV genome promoter. *J. Virol.* **73**, 251–259 (1999).
73. F. Radecke, P. Spielhofer, H. Schneider, K. Kaelin, M. Huber, C. Dotsch, G. Christiansen, M. A. Billeter, Rescue of measles viruses from cloned DNA. *EMBO J.* **14**, 5773–5784 (1995).
74. R. K. Plemper, A. L. Hammond, D. Gerlier, A. K. Fielding, R. Cattaneo, Strength of envelope protein interaction modulates cytopathicity of measles virus. *J. Virol.* **76**, 5051–5061 (2002).
75. P. Lieutaud, B. Canard, S. Longhi, MeDor: A metaserver for predicting protein disorder. *BMC Genomics* **9**, S25 (2008).
76. Z. Dosztányi, V. Csizmok, P. Tompa, I. Simon, IUPred: Web server for the prediction of intrinsically unstructured regions of proteins based on estimated energy content. *Bioinformatics* **21**, 3433–3434 (2005).
77. R. Linding, R. B. Russell, V. Neduva, T. J. Gibson, GlobPlot: Exploring protein sequences for globularity and disorder. *Nucleic Acids Res.* **31**, 3701–3708 (2003).
78. R. Linding, L. J. Jensen, F. Diella, P. Bork, T. J. Gibson, R. B. Russell, Protein disorder prediction: Implications for structural proteomics. *Structure* **11**, 1453–1459 (2003).

79. J. Prilusky, C. E. Felder, T. Zeev-Ben-Mordehai, E. H. Rydberg, O. Man, J. S. Beckmann, I. Silman, J. L. Sussman, FoldIndex: A simple tool to predict whether a given protein sequence is intrinsically unfolded. *Bioinformatics* **21**, 3435–3438 (2005).
80. A. Vullo, O. Bortolami, G. Pollastri, S. C. E. Tosatto, Spritz: A server for the prediction of intrinsically disordered regions in protein sequences using kernel machines. *Nucleic Acids Res.* **34**, W164–W168 (2006).
81. Z. R. Yang, R. Thomson, P. McNeil, R. M. Esnouf, RONN: The bio-basis function neural network technique applied to the detection of natively disordered regions in proteins. *Bioinformatics* **21**, 3369–3376 (2005).
82. B. Xue, R. L. Dunbrack, R. W. Williams, A. K. Dunker, V. N. Uversky, PONDR-FIT: A meta-predictor of intrinsically disordered amino acids. *Biochim. Biophys. Acta* **1804**, 996–1010 (2010).
83. D. T. Jones, D. Cozzetto, DISOPRED3: Precise disordered region predictions with annotated protein-binding activity. *Bioinformatics* **31**, 857–863 (2015).
84. M. Suyama, O. Ohara, DomCut: Prediction of inter-domain linker regions in amino acid sequences. *Bioinformatics* **19**, 673–674 (2003).
85. J. M. Chandonia, StrBioLib: A Java library for development of custom computational structural biology applications. *Bioinformatics* **23**, 2018–2020 (2007).
86. J. H. Hung, Z. Weng, Sequence alignment and homology search with BLAST and ClustalW. *Cold Spring Harb. Protoc.* **2016**, pdb.prot093088 (2016).
87. R. C. Edgar, MUSCLE: Multiple sequence alignment with high accuracy and high throughput. *Nucleic Acids Res.* **32**, 1792–1797 (2004).
88. *The PyMOL Molecular Graphics System, Version 1.8* (Schrödinger LLC, 2010).
89. K. B. Hummel, L. Lowe, W. J. Bellini, P. A. Rota, Development of quantitative gene-specific real-time RT-PCR assays for the detection of measles virus in clinical specimens. *J. Virol. Methods* **132**, 166–173 (2006).

Acknowledgments: We thank C. A. Rostad, M. Messner, and T. Kazarian for technical assistance at early stages of the study and J. Sourimant and A. L. Hammond for critical reading of the manuscript. Next-generation sequencing was carried out with the assistance of the Emory Integrated Genomics Core. **Funding:** This work was supported, in part, by U.S. Public Health Service grants AI083402 and AI071002 from the NIH/National Institute of Allergy and Infectious Diseases (to R.K.P.). **Author contributions:** R.M.C., S.A.K., and R.K.P. designed the experiments. All authors carried out the experiments. R.M.C., S.A.K., and R.K.P. performed the data analysis. R.M.C. and R.K.P. wrote the manuscript. **Competing interests:** The authors declare that they have no competing interests. **Data and materials availability:** All data needed to evaluate the conclusions in the paper are present in the paper. Additional data related to this paper may be requested from the authors.

Submitted 23 September 2016
Accepted 22 December 2016
Published 3 February 2017
10.1126/sciadv.1602350

Citation: R. M. Cox, S. A. Krumm, V. D. Thakkar, M. Sohn, R. K. Plemper, The structurally disordered paramyxovirus nucleocapsid protein tail domain is a regulator of the mRNA transcription gradient. *Sci. Adv.* **3**, e1602350 (2017).